



H₂ mass transfer – A key factor for efficient biological methanation: Comparison between pilot-scale experimental data, 1D and CFD models

Vincent Ngu^a, David F. Fletcher^b, John M. Kavanagh^b, Yan Rafrafi^a, Claire Dumas^a, Jérôme Morchain^a, Arnaud Cockx^{a,*}

^aToulouse Biotechnology Institute, Université de Toulouse, CNRS, INRAE, INSA, Toulouse, France

^bSchool of Chemical and Biomolecular Engineering, The University of Sydney, NSW 2006, Australia

HIGHLIGHTS

- Satisfactory numerical prediction of bioreactor performances using 1D and CFD models.
- Uniform porous plate leads to higher interfacial mass transfer.
- Analytical solutions unravel the impact of operating conditions on biological methanation efficiency.
- Sensitivity analysis reveals that CH₄ % increases with H₂ mass transfer but is not impacted by the absolute pressure.

ARTICLE INFO

Article history:

Received 16 June 2022

Received in revised form 28 November 2022

Accepted 9 December 2022

Available online 14 December 2022

Keywords:

Bubble column

Multiscale modeling

Gas-liquid mass transfer

Power-to-gas

CFD

Sparger

ABSTRACT

Biological methanation is an emerging Power-to-Gas technology that provides a flexible, efficient, and long-term storage system to address the renewable energy intermittency issue. However, scaling-up a biological methanation plant requires overcoming the bottleneck of H₂ gas-liquid mass transfer. The current work demonstrates analytically, experimentally and numerically the importance of H₂ mass transfer on CH₄ purity and productivity. The influence of sparger design was investigated in a pilot-scale bubble column bioreactor. An increase of 265 % in $k_L a$ and subsequently 81 % in CH₄ purity is obtained when a uniform porous plate is used over a 4-points porous sparger. Numerical simulation of the bioreactor was performed using a multiscale modeling approach coupling 1D and CFD models. The numerical simulations were validated satisfactorily by the experimental data. Parametric studies were also performed using the 1D model to reveal the impact of operating conditions on the bioprocess. An analytical solution for the productivity of biomethanation reactors at steady-state is proposed based on mass balances and provides new insights into biological methanation. It is found that any modification of operating parameters that improve H₂ mass transfer, such as higher gas recirculation rate and smaller bubble size, leads to a better bioreactor performance.

© 2022 Elsevier Ltd. All rights reserved.

1. Introduction

1.1. Background of biological methanation

In the past decades, global warming and climate change have become the centerpiece of discussion among policymakers. The Paris Climate Agreement sets the framework for participating countries to limit the temperature rise well below 2 °C. The European Commission has also set the goal of achieving a 32 % renewable energy share in the energy mix by 2030 (European Commission, 2016a, 2016b). Therefore, renewable energies play

an important role in mitigating the use of fossil fuels that have caused greenhouse gas emissions to reach a record high worldwide year-over-year. However, due to the intermittent behavior of renewable energy sources, such as wind and solar, an energy buffer is required. In this context, Power-to-Gas technologies play an important role in achieving deep decarbonization and ensuring a green transition of the global energy system from carbon-emitting fossil fuels to renewable energy sources. Biological methanation has emerged as an interesting option for Power-to-Gas application. The product – methane (CH₄) is a promising energy vector as it can be directly injected into the existing natural gas network for transport and storage.

Compared with catalytic methanation, biological methanation operates under milder conditions and methanogens have higher

* Corresponding author.

E-mail address: cockx@insa-toulouse.fr (A. Cockx).

Nomenclatures

Symbol	Description	Symbol	Description
a	Volumetric interfacial area, [m ² .m ⁻³]	u _{rel}	Relative velocity, [m.s ⁻¹]
C*	Solubility/equilibrium concentration, [mg.L ⁻¹]	u	Local phase velocity, [m.s ⁻¹]
C ₀	Distribution coefficient of the drift-flux model, [-]	u _c	Liquid circulation velocity, [m.s ⁻¹]
C _D	Drag coefficient, [-]	V	Reactor volume, [m ³]
C _G	Gas concentration, [mg.L ⁻¹]	y	Gas molar fraction, [-]
C _L	Liquid concentration, [mg.L ⁻¹]	Y _{A/B}	Conversion yield of A on B, [g _A .g _B ⁻¹]
D _i	Species diffusivity, [m ² .s ⁻¹]	z	Axial coordinate, [m]
d ₃₂	Sauter mean diameter, [m]	<i>Greek symbols</i>	
d _b	Bubble diameter, [m]	Symbol	Description
D _G	Gaseous axial dispersion coefficient, [m ² .s ⁻¹]	ε	Local phase holdup, [-]
D _L	Liquid axial dispersion coefficient, [m ² .s ⁻¹]	η	H ₂ conversion, [-]
D _r	Reactor diameter, [m]	μ	Dynamic fluid viscosity, [Pa.s]
F _i	Species gas molar flowrate, [mol.s ⁻¹]	ν	Kinematic fluid viscosity, [m ² .s ⁻¹]
g	Gravity acceleration, [m.s ⁻²]	ρ	Fluid density, [kg.m ⁻³]
H	Reactor height, [m]	σ	Surface tension, [N.m ⁻¹]
He	Henry's constant, [mg.L ⁻¹ .Pa ⁻¹]	φ _{H₂}	Specific hydrogen uptake rate, [g _{H₂} .g _X ⁻¹ .h ⁻¹]
H ^{cc}	Dimensionless Henry solubility, [-]	φ _{bio}	Specific uptake rate set by biological uptake capacity, [g _{H₂} .g _X ⁻¹ .h ⁻¹]
j _G	Superficial gas velocity, [m.s ⁻¹]	φ _{phy}	Specific uptake rate set by physical substrate transport, [g _{H₂} .g _X ⁻¹ .h ⁻¹]
j _L	Superficial liquid velocity, [m.s ⁻¹]	φ	Local volumetric molar fluxes, [mg.L ⁻¹ .s ⁻¹]
K	Biological affinity constant, [mg.L ⁻¹]	<i>Subscripts and superscripts</i>	
k _L	Liquid side mass transfer coefficient, [m.s ⁻¹]	Symbol	Description
k _{L,a}	Volumetric mass transfer coefficient, [s ⁻¹]	0	Inlet defined at the reactor domain
m	Maintenance rate, [g _{H₂} .g _X ⁻¹ .h ⁻¹]	G	Gaseous phase
M	Molar mass, [g.mol ⁻¹]	i	Species
MPR	Methane production rate per unit volume of reactor, [mL.CH ₄ .L ⁻¹ .h ⁻¹]	in	Fresh feed inlet
P	Pressure, [Pa]	k	Phase
q	Specific bioreaction rate, [g _{H₂} .g _X ⁻¹ .h ⁻¹]	L	Liquid phase
q _{H₂} ^{max}	Maximum specific hydrogen uptake rate, [g _{H₂} .g _X ⁻¹ .h ⁻¹]	out	Outlet
Q _G	Gas volumetric flowrate, [m ³ .s ⁻¹]	<i>Dimensionless numbers</i>	
Q _r	Gas recirculation flowrate, [m ³ .s ⁻¹]	Symbol	Description
Q _{tot}	Total gas flow rate, (Q _{G,in} + Q _r) [m ³ .s ⁻¹]	Eo	Eötvös number
R	Ideal gas constant, [J.mol ⁻¹ .K ⁻¹]	Mo	Morton number
R _i	Species reaction term per unit volume of liquid, [mg _i .L ⁻¹ .s ⁻¹]	Re	Reynolds number
S	Cross-section area, [m ²]		
r	Reaction rate vector, [g _{H₂} .L ⁻¹ .h ⁻¹]		
T	Temperature, [K]		
t	Time, [s]		
T _i	Species mass transfer rate, [mol.s ⁻¹]		

resistance to feed gas impurities, which lower the CH₄ production costs (Jensen et al., 2021). Besides interconnecting with the renewable energy electricity grid, biological methanation can be integrated with wastewater treatment plants (WWTP) and anaerobic digestors, such as the biological methanation plant on BIOFOS site in Avedøre, Denmark (Lardon et al., 2018). Additionally, the H₂ produced from the electrolysis of water, oxygen (O₂) can be fed to nearby WWTP. The biogas from anaerobic digestion containing mainly CH₄ and carbon dioxide (CO₂) can be upgraded by biological methanation. The heat produced from biological methanation can be used to heat the anaerobic digester. Such synergistic effects between industries have shown that a positive energy balance is achievable at large-scale (Lardon et al., 2018).

1.2. Progress in biological methanation study

Despite numerous advantages of biological methanation, the overall process is strongly limited by hydrogen (H₂) mass transfer, as agreed by several researchers (Lecker et al., 2017; Rafrafi et al., 2020; Rusmanis et al., 2019). Only a few large-scale biological methanation plants with a range of volume between 3.5–100 m³

are referenced in the literature, signifying that the technology is only at the early stage of its commercial application (Rafrafi et al., 2020). Extensive investigations on reactor design, system configurations and operating conditions are still mainly at the laboratory or pilot-scale. Several reactor designs, such as stirred tank reactors (Figueras et al., 2021; Martin et al., 2013; Peillex et al., 1990), bubble column reactors (Bassani et al., 2017; Kougias et al., 2017; Laguillaumie et al., 2022; Voelklein et al., 2019), membrane reactors (Díaz et al., 2015; Luo and Angelidaki, 2013), fixed-bed reactors (Lee et al., 2012) and trickled bed reactors (Markthaler et al., 2020; Sieborg et al., 2020; Strübing et al., 2018; Ullrich et al., 2018), have been studied to demonstrate the feasibility of biological methanation. Different strategies for the operating configurations and conditions have been investigated to improve H₂ mass transfer efficiency (Bassani et al., 2017; Kougias et al., 2017; Ullrich and Lemmer, 2019). Two main configurations, namely in-situ and ex-situ biological methanation strategies are also reported (Angelidaki et al., 2018; Jensen et al., 2021; Lecker et al., 2017; Rafrafi et al., 2020). For the in-situ system, H₂ is directly injected into an anaerobic plant to increase biogas production through CO₂ consumption. Meanwhile, for the ex-situ system, H₂ and bio-

gas or any CO₂ source are injected into another independent bioreactor for biogas upgrading through biological methanation. As most of the studies focus on experimental work, the development of numerical models is also necessary to elucidate the bioprocess and predict bioreactor performances. Therefore, extensive research and development is required to better understand the fundamental phenomena and the coupling in a biological methanation reactor in order to guide the scale-up of the technology. The multiphysics phenomena to couple in the numerical model include:

- Two-phase gas–liquid bubbly flow.
- Multi-species mass transfer (H₂, CO₂, CH₄).
- Biological kinetics.

In terms of biokinetics, the classical Monod-type law is not appropriate to describe biological methanation reaction, as discussed in Ngu et al. (2022). When bioreaction is limited by mass transfer, the dissolved substrate concentration reaches zero, consequently, the Monod-type description forces the reaction to stop, but the mass transfer flux is still maintained. As the limiting factor of biological methanation is H₂ mass transfer, the detailed bioreaction description becomes less important (Markthaler et al., 2020). Therefore, a more practical and realistic model capable of switching between the biological and physical limited regime is necessary, especially when multiphysics phenomena are competing. In addition, computational fluid dynamics (CFD) models for biological methanation are still scarce in the literature and they mostly focus on the hydrodynamic behavior of bioreactors (Leonzio, 2016; Markthaler et al., 2020). Leonzio (2018, 2016) presents a CFD model to study the mixing and the mass transfer efficiency of in-situ biological methanation in a stirred tank reactor but no discussion on the bioreaction is provided. Meanwhile, liquid gas holdup of a lab-scale trickled bed bioreactor is predicted satisfactorily by the CFD model of Markthaler et al. (2020) but the biomethane production is underpredicted. In fact, a CFD model can unravel local flow structures precisely, hence, it can offer a good description of hydrodynamic coupling with mass transfer and bioreaction. Here, we attempt to develop a CFD model that considers the mutual interactions of multiphase bubbly flow, multispecies mass transfer and biological reaction with the validation from biological methanation experimental data presented in Rafrafi et al. (2019).

1.3. Importance of sparger design

The sparger design is very important as it largely determines the initial bubble size, and thus the bubble rise velocity (Kulkarni and Joshi, 2011). Different types of sparger design have been studied in the literature to determine the hydrodynamics and mass transfer properties, such as tree sparger, ring sparger, spider sparger, porous plate, perforated plate, and needle sparger. These spargers can be classified into two major categories: plate type spargers and pipe type spargers (Kulkarni and Joshi, 2011). At a given superficial gas velocity, these spargers will produce different flow regimes, depending on the uniformity of gas injection, the pore size, and the number of holes (Besagni et al., 2018; Sharaf et al., 2016; Veera and Joshi, 1999). Consequently, the flow pattern will impact the mass transfer and (bio)reaction rate (Li et al., 2021). In aerobic bioprocesses, the sparger plays an important role in supplying gas substrate to the biomass for growth and metabolism. For example, oxygen transfer is pivotal for wastewater treatment and aeration remains the major operating cost of such processes (Amaral et al., 2019; Fayolle et al., 2007). In biological methanation whereby the major substrates (H₂ and CO₂) are fed through the gaseous phase, the overall process can be limited by H₂ mass transfer. This is due to the poor solubility of H₂ (of the order 1 mg/L at

atmospheric pressure compared with that of O₂ at 40 mg/L). To elucidate the importance of H₂ mass transfer, the hydrodynamics of two sparger designs and their impact on biological methanation are studied.

1.4. Objective of this work

In this work, ex-situ biological methanation is studied experimentally and numerically in a pilot-scale bubble column bioreactor. In the same bubble column, the importance of the gas sparger system on the global hydrodynamics and the bioreactor performances was also demonstrated. Besides, a one-dimensional (1D) spatio-temporal multi-species mass transfer model considering bubble size changes due to pressure and mass transfer coupled with a newly proposed bioreaction closure model was applied to study the experimental system. The model was validated using experimental data and it can be used to identify certain key parameters for the optimization of the industrial-scale bubble column design for biological methanation through a series of sensitivity analyses. CFD simulations were also carried out to investigate the local hydrodynamics and the bioreactor performances equipped with two types of gas sparger. Lastly, an analytical solution based on gaseous mass balances at steady-state is proposed. It underlines the importance of mass transfer to the bioprocess. The objectives of this multiphysics modeling are threefold: to highlight the importance of sparger design on bioreactor performance, to perform numerical predictions of bioreactor performance using 1D and CFD models, and to identify underlying parameters impacting H₂ mass transfer. This work aims at offering some guidelines for bubble column bioreactor design, and thus to accelerate the biological methanation technology transfer to the industry.

2. Experimental and numerical methods

2.1. Experimental setup

The experiment setup as shown in Fig. 1(a) is composed of a 22 L bubble column with an initial liquid height and internal diameter of 1200 mm and 150 mm, respectively. The experiment was conducted at atmospheric pressure and in thermophilic conditions (temperature at 328.15 K). The temperature was regulated with a thermostat (LAUDA®) by circulating water in the jacket of the bubble column. H₂:CO₂ with a ratio of 4:1 was fed to the column with any unreacted gas being recirculated at a high rate (Q_r) of 2 NL/min to increase the hydrogen conversion. Two types of gas sparger, presented in Fig. 1(b) and (c), were tested experimentally. The first, named the 4-points porous sparger, is composed by 4 small glass sintered diffusers with a diameter of 10 mm each. The second, a uniform porous plate, consists of a single porous sintered diffuser occupying the bottom cross-section of the column. Both spargers have the same properties with a pore size between 100 and 160 μm. The total area of the spargers is 0.000314 and 0.0177 m² for the 4-points sparger and porous plate, respectively. The inlet gas flowrate ($Q_{G,in}$) was varied between 0.001 and 0.16 NL/min. The influence of uniform and non-uniform aeration is discussed in Section 3.3.

The bubble diameter is required for the 1D and CFD models. However, it is not determined under bioreaction conditions, as it cannot be measured by optical means due to the turbid and muddy liquid medium. The bubble diameter was measured in air-tap water system and was used as an estimate of the inlet bubble diameter for the numerical models. A camera was installed at the column mid-height to measure the bubble size. The details on the bubble size measurement can be found in Ngu et al. (2022).

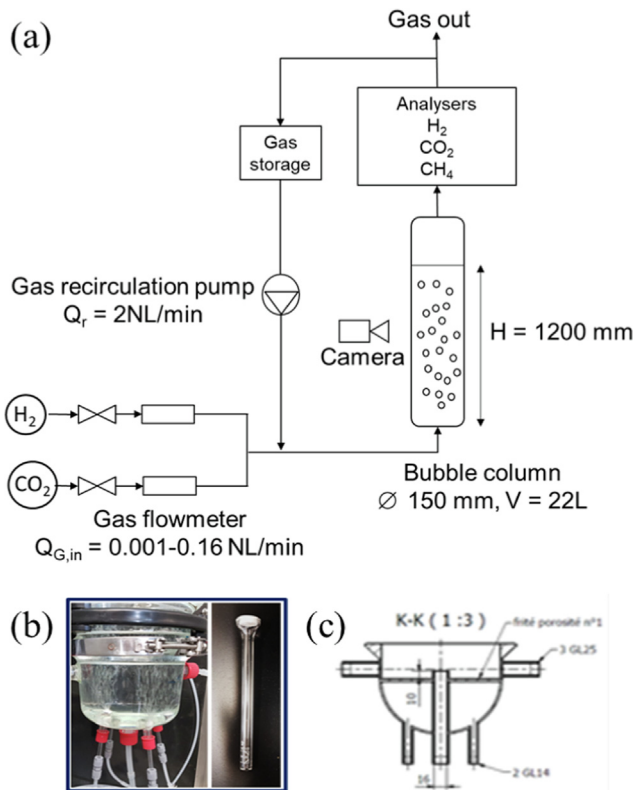


Fig. 1. (a) Simplified experimental setup. (b) 4-points sparger (c) Porous plate.

Fig. 2(a) and (b) show that the bubbles formed using the 4-points sparger are larger than those from the porous plate. This shifts the bubble size distribution to larger sizes, resulting in a larger Sauter mean diameter, as shown in Fig. 2(c) and (d). The bubble diameter used for the simulations is discussed in Section 2.3.

To characterize the bioreactor performances, two parameters were chosen, namely outlet methane gas purity ($y_{\text{CH}_4,\text{out}}$) and methane production rate (MPR). MPR is defined in equation (1) as the outlet methane volumetric flowrate per unit volume of reactor. These two parameters represent the quality and the quantity of methane contained in the off-gas.

$$\text{MPR} = \frac{y_{\text{CH}_4,\text{out}} Q_{G,\text{out}}}{V} \quad (1)$$

where $Q_{G,\text{out}}$ is outlet gas flowrate and V is the reactor volume.

2.2. 1D model for multispecies bioreactive bubbly flow

A previously developed 1D model was applied in this work and is presented briefly here. The numerical discretization and the applied scheme were kept the same as in Ngu et al. (2022). The 1D model consists of the following species transport equations (equations (2) and (3)), referring to the conservation of mass in an elementary volume of height dz . The resolution of this model provides the spatial and temporal profiles of gas holdup and species concentrations in both phases.

$$\frac{\partial \phi_{G,i}}{\partial t} + \frac{\partial u_G \phi_{G,i}}{\partial z} = D_G \frac{\partial}{\partial z} \left(\varepsilon_G \frac{\partial C_{G,i}}{\partial z} \right) - k_{L,i} a (C_i^* - C_{L,i}) \quad (2)$$

$$\frac{\partial \phi_{L,i}}{\partial t} + \frac{\partial u_L \phi_{L,i}}{\partial z} = D_L \frac{\partial}{\partial z} \left(\varepsilon_L \frac{\partial C_{L,i}}{\partial z} \right) + k_{L,i} a (C_i^* - C_{L,i}) + \varepsilon_L R_i \quad (3)$$

$$\varepsilon_G + \varepsilon_L = 1 \quad (4)$$

The key parameters of this model are u_G and u_L , the gas and liquid velocities, respectively. ε_G and ε_L are the gas and liquid holdup, summing to one, as stated in equation (4). $C_{G,i}$ and $C_{L,i}$ are the concentration of species i : mass per unit volume of the gas and liquid phase, respectively. Hence, $\phi_{G,i}$ is the concentration of species i in the gas phase: mass per unit volume of the column, i.e., $\phi_{G,i} = \varepsilon_G C_{G,i}$. Similarly, we have $\phi_{L,i} = \varepsilon_L C_{L,i}$. The liquid axial dispersion coefficient, D_L , was calculated from the correlation proposed by Deckwer et al. (1974), as presented in equation (5) while the gaseous axial dispersion coefficient, D_G , was estimated from the correlation of Wachi and Nojima, (1990), as written in equation (6). Both correlations are function of the superficial gas velocity, j_G , and bubble column diameter, D_r .

$$D_L = 2.7 \cdot 10^{-4} \cdot (D_r \cdot 100)^{1.4} \cdot (j_G \cdot 100)^{0.3} \quad (5)$$

$$D_G = 20 \cdot D_r^{1.5} \cdot j_G \quad (6)$$

The local volumetric interfacial area for mass transfer, a , was calculated from the local bubble diameter, d_b , and gas holdup, ε_G , as expressed in equation (7). The liquid side mass transfer coefficient of each species $k_{L,i}$ was computed via equation (8) from Higbie (1935) and it involves the species dependent liquid-side diffusion coefficient, D_i , and the spatially dependent variables (ε_G , d_b , u_{rel}), with $u_{\text{rel}} = u_G - u_L$ the homogeneous slip velocity, as presented in equation (9).

$$a = 6 \frac{\varepsilon_G}{d_b} \quad (7)$$

$$k_{L,i} = 2 \sqrt{\frac{D_i u_{\text{rel}}}{\pi d_b}} \quad (8)$$

The corresponding diffusion coefficients at 328.15 K are 1×10^{-8} , 4.5×10^{-9} , and $3.3 \times 10^{-9} \text{ m}^2 \cdot \text{s}^{-1}$ for hydrogen, carbon dioxide and methane, respectively (Thibodeaux and Mackay, 2010).

The calculation of the gas and liquid phase velocities is crucial in the 1D model as they impact the gas holdup. In uniform gas injection system, the hydrodynamics description in the 1D model is more straightforward. The bubble column operated in batch mode ($u_L = 0$), therefore, the bubbles ascend in a uniform manner and the bubbly flow can be modeled using the bubble terminal velocity, u_{rel} , as shown in equation (9). The drag coefficient C_D for contaminated system proposed by Tomiyama et al. (1998) was applied, as expressed in equation (10).

$$u_{\text{rel}} = \sqrt{\frac{4 g (\rho_L - \rho_G) d_b}{3 \rho_L C_D}} \quad (9)$$

$$C_D = \max \left\{ \frac{24}{\text{Re}} (1 + 0.15 \text{Re}^{0.687}), \frac{8}{3} \frac{\text{Eo}}{(4 + \text{Eo})} \right\}$$

$$\text{Re} = \frac{u_{\text{rel}} d_b}{\nu_L} \quad \text{Eo} = \frac{(\rho_L - \rho_G) g d_b}{\sigma} \quad (10)$$

g is the acceleration due to gravity ($9.81 \text{ m}^2 \cdot \text{s}^{-1}$), ρ_L and ρ_G are the liquid and gas density, respectively, Re is the Reynolds number and Eo is the Eötvös number. The viscosity and density of water were corrected to 328.15 K, whilst the surface tension of water at 293.15 K was applied which yields $\rho_L = 985 \text{ kg} \cdot \text{m}^{-3}$, $\mu_L = 5.10^{-4} \text{ Pa} \cdot \text{s}$, and $\sigma = 0.072 \text{ N} \cdot \text{m}^{-1}$.

In the non-uniform gas injection system, a non-uniform hydrodynamics profile was observed due to complex gas and liquid circulation flow. Therefore, the bubble velocity was modeled using the drift-flux approach, expressed as.

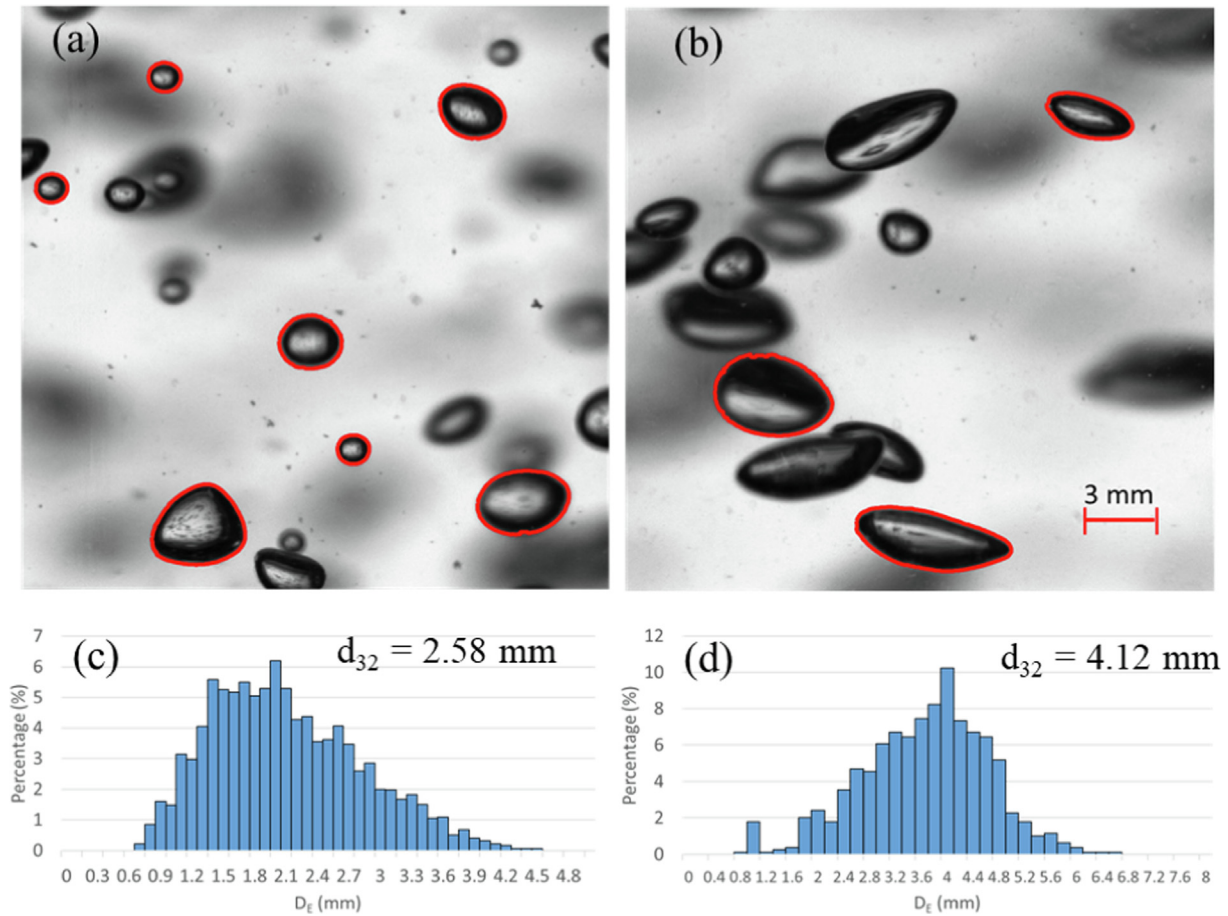


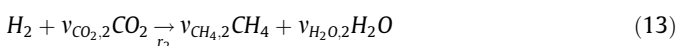
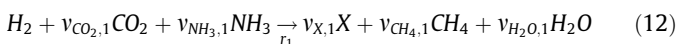
Fig. 2. (a and b) Detected bubbles by the image processing algorithm at $Q_{G,in} = 1.6$ NL/min. (c and d) Histogram of bubble size distribution for a bin size of 0.2 mm equivalent diameter and the calculated Sauter mean diameter. (a) and (c) porous plate, (b) and (d) 4-points sparger.

$$u_G = C_0 \langle j \rangle + u_{rel} \quad (11)$$

The distribution coefficient C_0 describes the non-uniform flow profile and it is calculated from its definition $C_0 = \frac{\langle e_{G,j} \rangle}{\langle e_G \rangle \langle j \rangle}$ (Zuber and Findlay, 1965). $\langle j \rangle$ is the averaged mixture volumetric flux which is the sum of the superficial gas and liquid velocities $\langle j_G + j_L \rangle$. The liquid circulation velocity, u_c , was considered as j_L . Information on C_0 and u_c were obtained from the resolved 3D CFD simulation, as in Cockx et al. (1997) and Talvy et al. (2007). Further discussions on the hydrodynamics are reported in Section 3.2 and Table 3.

In short, the detailed spatially resolved CFD model provides the fluid flow pattern in terms of simplified hydrodynamics parameters (C_0 , u_c) to the 1D model, as depicted in Fig. 3. This multiscale modeling approach is similar to the workflow proposed by Bauer and Eigenberger (1999) and Cockx et al. (1997) for bubble columns and loop reactors. This approach is useful when non-homogeneities in the flow are generated by the non-uniform gas sparger.

The calculation of the reaction rates, R_i , follows the previous work of Ngu et al. (2022) and is briefly presented here. It is based on the magnitude of the hydrogen uptake rate, φ_{H_2} , and the set of intracellular reactions describing the conversion of H_2 and CO_2 into CH_4 proposed by Schill et al. (1996):



The metabolic flux-based model is based on the computation of the reaction rate vector $\mathbf{r} = \{r_1, r_2, r_3\}$ in $g_{H_2} \cdot L^{-1} \cdot h^{-1}$. r_1 , r_2 , and r_3 signify growth, maintenance and death mechanisms, respectively, experienced by the biomass at different stage of its lifecycle, depending on the local availability of the substrates. The hydrogen uptake is used for growth and maintenance activity, such that $r_1 + r_2 = \varphi_{H_2}X$. The priority is given to the specific maintenance rate, m , consequently two scenarios can be identified (i) $\varphi_{H_2} > m$ and (ii) $\varphi_{H_2} < m$. For the first case, the maintenance requirement is reached and therefore growth is ensured, and death is negligible, thus, $r = \{\varphi_{H_2} - m, m, 0\}X$. Otherwise, in the second case, growth halts as the hydrogen supply is insufficient for maintenance. The maintenance rate is now defined by φ_{H_2} and the cell death rate is proportional to the energy lacking for maintenance, thus, $r = \{0, \varphi_{H_2}, m - \varphi_{H_2}\}X$.

The calculation of the hydrogen specific uptake rate φ_{H_2} is presented in equation (15). It uses a standard approach in multiphase reactor modeling, which is to define the actual consumption rate as the smallest (limiting) rate between the biological uptake rate and the external physical transport rate (Ngu et al., 2022; Pigou and Morchain, 2015).

$$\varphi_{H_2} = \min\{\varphi_{bio}, \varphi_{phy}\} \quad (15)$$

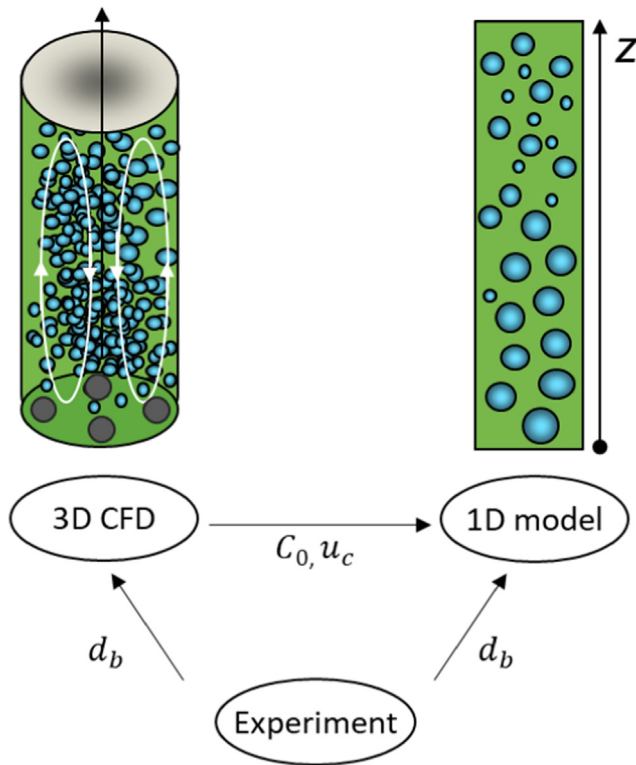


Fig. 3. Workflow to predict bioreactor performances using 1D model coupled with CFD model.

The biological uptake capacity is calculated from the Monod model, involving the maximum specific hydrogen uptake capacity $q_{H_2}^{max}$, the saturation constant K_{H_2} , and the liquid phase hydrogen concentration C_{L,H_2} :

$$\varphi_{bio} = q_{H_2}^{max} \frac{C_{L,H_2}}{K_{H_2} + C_{L,H_2}} \quad (16)$$

The physical transport rate involves two phenomena in parallel: the gas–liquid mass transfer rate and the micromixing rate at the cell scale. The specific substrate flux supplied to the cell is thus calculated as the larger of the two rates:

$$\varphi_{phy} = \max \left(\frac{k_L a (C_{L,H_2}^* - C_{L,H_2})}{\varepsilon_L X}, \frac{C_{L,H_2}}{X \tau_m} \right) \quad (17)$$

This formulation provides a physically consistent and numerically stable way to handle the situation when the biological methanation is limited by H_2 mass transfer whereby the dissolved H_2 concentration approaches zero.

The reaction terms for each species R_i in equation (3) is summarized in equations (18)–(21):

$$R_{H_2} = (r_1 + r_2) = \varphi_{H_2} X \quad (18)$$

$$R_{CO_2} = (Y_{CO_2/H_2} r_1 + Y_{CO_2/H_2}^m r_2) \quad (19)$$

$$R_{CH_4} = (Y_{CH_4/H_2} r_1 + Y_{CH_4/H_2}^m r_2) \quad (20)$$

$$R_X = Y_{X/H_2} (r_1 - r_3) \quad (21)$$

with $Y_{i/j}$ being the yield coefficient in grams of i per gram of j consumed. The values for the biological methanation kinetic rates and yield coefficient are reported in Ngu et al. (2022) and the same values are applied in this work.

2.3. CFD Eulerian model setup for multispecies bubbly flow

3D CFD simulations were performed using the commercial CFD code ANSYS Fluent® version 2021R1. The simulations were based on the Euler-Euler two fluid model, that solves the Reynolds-Averaged Navier-Stokes (RANS) equations. Turbulence was modeled using the standard $k-\varepsilon$ model. Both phases were mixtures to investigate the concentration of each species. The closure relations required to complete the model are summarized in Table 1. In this work, the virtual mass and wall lubrication forces were neglected. It has been shown that the virtual mass force has no significant influence in bubble column reactors as the bubbles quickly reach its terminal velocity (Deen et al., 2001; McClure et al., 2014; Tabib et al., 2008). The wall lubrication force is important for the near wall layer only if significant number of bubbles lie inside the boundary layer, as in the case for nucleate boiling, and thus it is also neglected here.

The liquid phase was water with the density and surface tension described in Section 2.2. For the CFD model, the gas recycling was simulated by a pseudo-steady state, with a total gas flow (Q_{tot}) defined as the sum of inlet gas flowrate ($Q_{G,in}$) and gas recirculation flow rate (Q_r). The composition of the gas at the inlet was determined using the 1D model. For example, Q_{tot} for the reference case corresponds to 2.14 NL/min. The gas phase was considered as an ideal gas with a constant bubble diameter. No bubble coalescence or breakage were considered as the gas holdup was below 1 % as previously measured in air–tap water system in Ngu et al. (2022). Experimentally measured bubble size in air–tap water system serves as an estimate of the inlet bubble diameter for both the 1D and CFD models. For the reference case ($Q_{tot} = 2.14$ NL/min) the inlet bubble diameter for porous plate and 4-points sparger were set and assumed constant as 2 mm and 5 mm, respectively. Using the bubble diameter correlation of Abro et al. (2021) developed for porous sparger yields 1.7 mm for a gas flow of 2.14 NL/min, which corresponds well with the estimated 2 mm used for the porous plate. To elucidate the impact of bubble diameter, a sensitivity analysis on the bubble diameter was also performed and is presented in Section 3.5.

For the boundary conditions, all walls were set as no-slip condition for the liquid and free-slip for the gas. Gas entering through the inlet was modeled using a velocity-inlet boundary condition. The total gas flowrate Q_{tot} was set at the inlet, with the velocity magnitude set as the bubble terminal velocity of the imposed bubble diameter calculated using the Tomiyama et al. (1998) drag model. A turbulence intensity of 5 % and a turbulent viscosity ratio of 10 were imposed at the inlet. The column outlet was modeled as an opening at zero gauge pressure, with a complete back-flow of gas, followed the suggestion of Nadal-Rey et al. (2022). The inlet composition of the gas phase followed that of 1D model. The inlet species mole fraction ratio of $H_2:CO_2:CH_4$ were 17.4%:2.5%:80.1% and 49.8%:5.6%:44.6% for the porous plate and 4-points sparger, respectively.

The solution strategy is detailed as follow. The hydrodynamics were first solved with the interphase forces presented in Table 1. Once the hydrodynamics converged, the species transport equations were then solved, determining the transport of gaseous species throughout the column. Lastly, all equations were solved

Table 1
Summary of interfacial force correlations used in the CFD model.

Force	Correlation
Drag	(Tomiyama et al., 1998)
Lift	(Tomiyama et al., 2002)
Turbulent dispersion	(Simonin and Viollet, 1990)

simultaneously to capture the coupling between hydrodynamics, mass transfer and bioreaction. Species transport equations were also solved to couple mass transfer and bioreaction with the bubbly flow. Given the short simulation time, the growth of biomass is negligible, thus the biomass concentration was not solved but was fixed set at 0.1 kg.m^{-3} . User-defined functions (UDFs) were developed to describe $k_{L,i}$ and R_i as expressed in equations (8) and (18).

The Phase Coupled SIMPLE scheme was used for pressure–velocity coupling. The first-order implicit temporal discretization scheme was used. For the spatial discretization schemes, QUICK was used for density and volume fraction, the first-order upwind scheme was used for the turbulence variables, and the second-order upwind scheme was used for the momentum and species transport equations. The scaled residual targets were set to 10^{-5} and a time step of 0.001 s with a maximum of 10 iterations per step were employed. Hydrodynamic simulations were run for a time of 20 s. An extra 10 s were run for the species transport equations. After all species in the gaseous phase are transported, the mass transfer together with bioreaction simulation were run for 20 s. The global mass balances for the gas phase were also assessed.

For the porous plate, direct comparison with the experimental data was carried out without performing CFD simulations in advance. For the 4-points sparger, CFD simulation was performed beforehand to obtain the fluid flow pattern and this information (C_0 and u_c) was then fed into the 1D model. The hydrodynamics was studied first and subsequently the bioreactor performance was compared with that of the 1D model. The goal was to compare the bioreactor performances ($y_{\text{CH}_4, \text{out}}$ and MPR) obtained from the two models with the experimental data from Raftafi et al. (2019).

3. Results and discussions

The hydrodynamic behavior of the two spargers is first evaluated using both the 1D and CFD models and the results of both models are then compared in terms of global gas holdup. To rectify the drawback of the 1D model in the hydrodynamic description of 4-points sparger, information from the CFD model is extracted and fed into the 1D model, as discussed in Section 2.2.

3.1. Mesh convergence

For the porous plate, a swept mesh is used throughout the geometry. For the 4-points sparger, high gradients are expected near the inlet due to non-uniform gas injection. From the gas inlet up to a height of 3-column diameter, the poly-hexcore mesh is more refined, with a polyhedral transition layer between the two jet formation zones. After the 3-column diameter height, a coarser mesh is employed in the column center with polyhedral elements near the wall.

Table 2 shows that the difference in gas holdup between the coarse and fine mesh for both spargers is relatively small. In both cases, a very low gas holdup ($<1\%$) was obtained as the superficial gas velocity is low. The two-phase bubbly flow ingenerated by the porous plate is expected to be uniform with no significant gradients. It is not surprising to obtain very close gas holdups for the

two meshes. To optimize the computational time, the coarse mesh for both spargers, as presented in Fig. 4, was used in this work.

3.2. Extracting hydrodynamics parameters from the CFD model

Fig. 5 depicts the gas holdup and gas velocity contour profiles obtained from CFD model for both spargers. Fig. 5(a) and (c) show that the bubbly flow using the porous plate is rather uniform radially, which is a typical characteristic of homogeneous flow regime at this low superficial gas velocity. A slight increase of 8 % in the gas holdup is observed from the inlet to the free surface, due to a decrease of pressure in the axial direction, in line with the ideal gas law. Fig. 5(b) and (d) reveal the complex local flow structure created by the 4-points sparger. It is found that the 4-points sparger creates strong jets, which gives rise to high radial gradients at the bottom of the column which gradually homogenize at the top of the column.

Fig. 6(a) shows that the radial profile of gas holdup for the porous plate is rather flat at the bottom of the column ($z/H = 0.25$). The liquid velocity is almost zero for the porous plate case, signifying a very weak liquid recirculation effect, as shown in Fig. 6(b). At the same zone, the 4-points sparger case shows a non-uniform gas holdup profile. For the 4-points sparger case, higher gas holdup is located away from the center, as the local gas injection is located near the wall. This effect diminishes with height, where a developed flow region occurs (see cross section contours in Fig. 5(b) and (d)). The liquid is dragged upwards by the bubbles near the wall and recirculates downwards in the centre, as shown by the

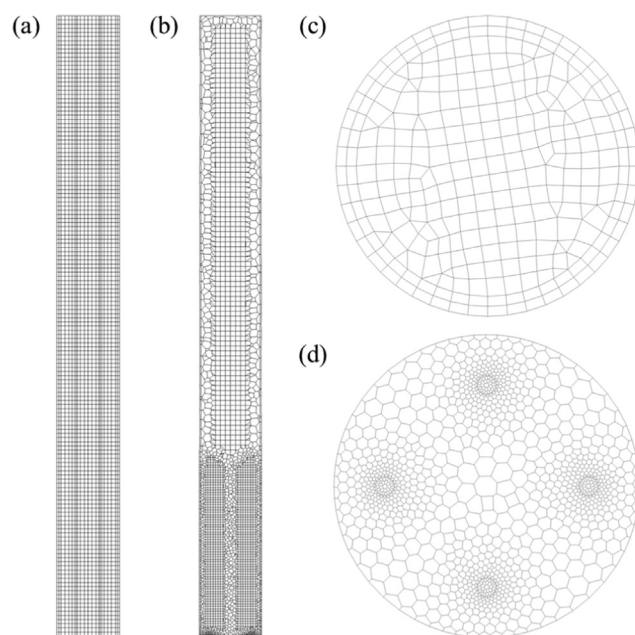


Fig. 4. Axial and radial section of the coarse mesh. (a and c) porous plate (b and d) 4-points sparger.

Table 2

Impact of grid size on the gas holdup for both spargers with the same superficial gas velocity of 0.136 cm.s^{-1} .

	Porous plate ($d_b = 2 \text{ mm}$, $u_G = 0.29 \text{ m.s}^{-1}$)		4-points sparger ($d_b = 5 \text{ mm}$, $u_G = 0.24 \text{ m.s}^{-1}$)	
	Coarse mesh	Fine mesh	Coarse mesh	Fine mesh
Number of elements	44,700	494,000	46,500	561,000
Typical element size (mm)	8	4	8	4
Gas holdup (%)	0.547	0.546	0.580	0.575

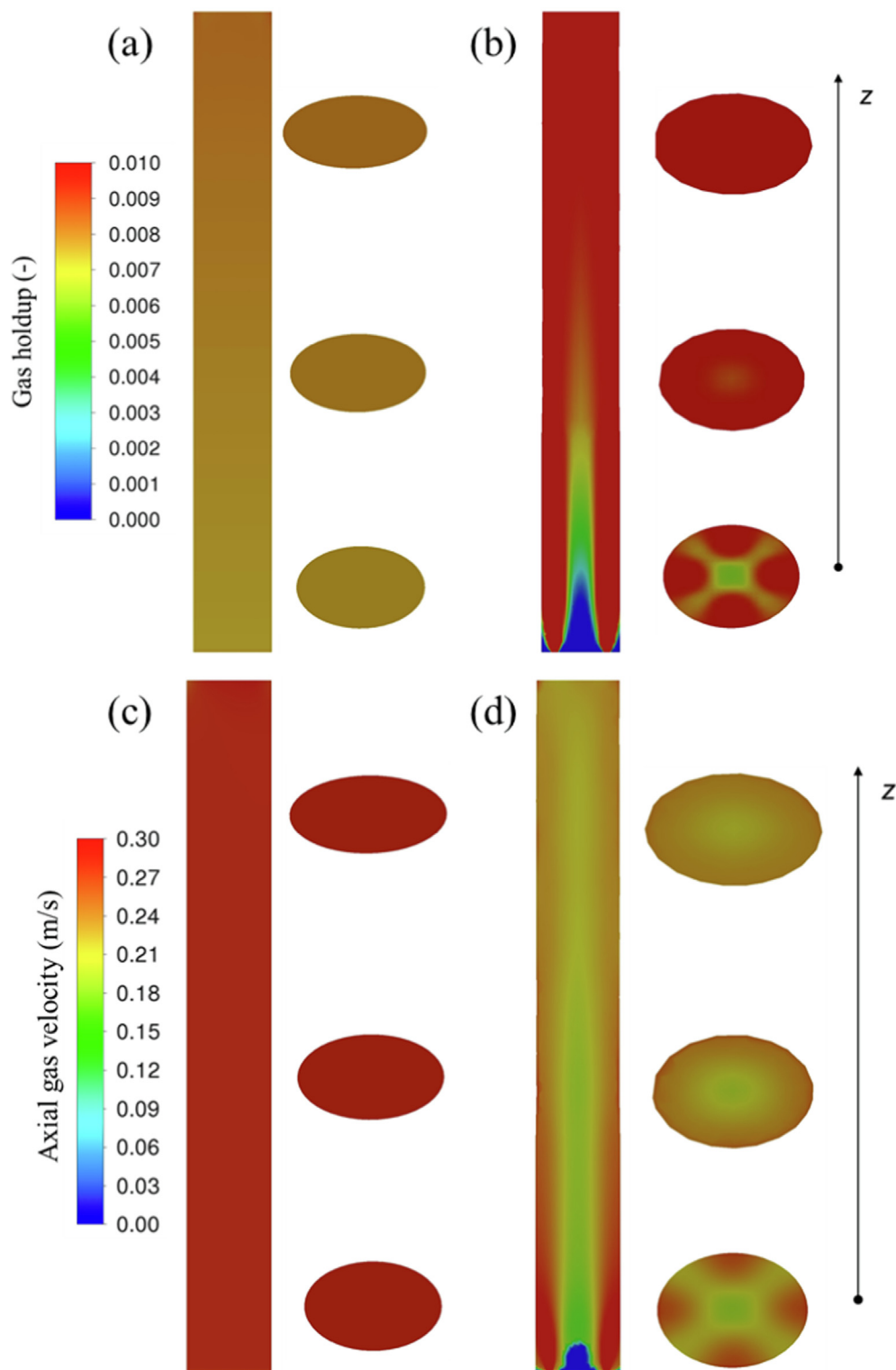


Fig. 5. Contours of the gas hold-up (a and b) and axial gas velocity component (c and d) in a vertical plane passing through center and three cross sections ($z/H = 0.25, 0.5, \text{ and } 0.75$) for the reference case. (a) and (c) porous plate, (b) and (d) 4-points sparger.

axial liquid velocity profile (Fig. 6(b)). Fig. 6(c) shows the large-scale recirculation structures due to non-uniformities in the aeration is captured by the CFD model near the inlet, which is also observed experimentally by Hartevelde et al. (2003). The authors observed a static recirculation cell near the bottom of the column when the gas distributor was located at the wall, similar to the 4-points sparger whereby the bubbles are introduced near the wall.

Table 3 presents the overall hydrodynamics results. Under complex hydrodynamics conditions with large-scale coherent structures encountered in the 4-points sparger case, an axial hydrodynamics description is not sufficient. To tackle this issue, fluid flow information from the CFD model is provided to the 1D model in terms of simplified hydrodynamics (C_0 and u_c) as described in the workflow in Fig. 3. The drift-flux coefficient C_0 is estimated from the local hydrodynamics profile using its definition

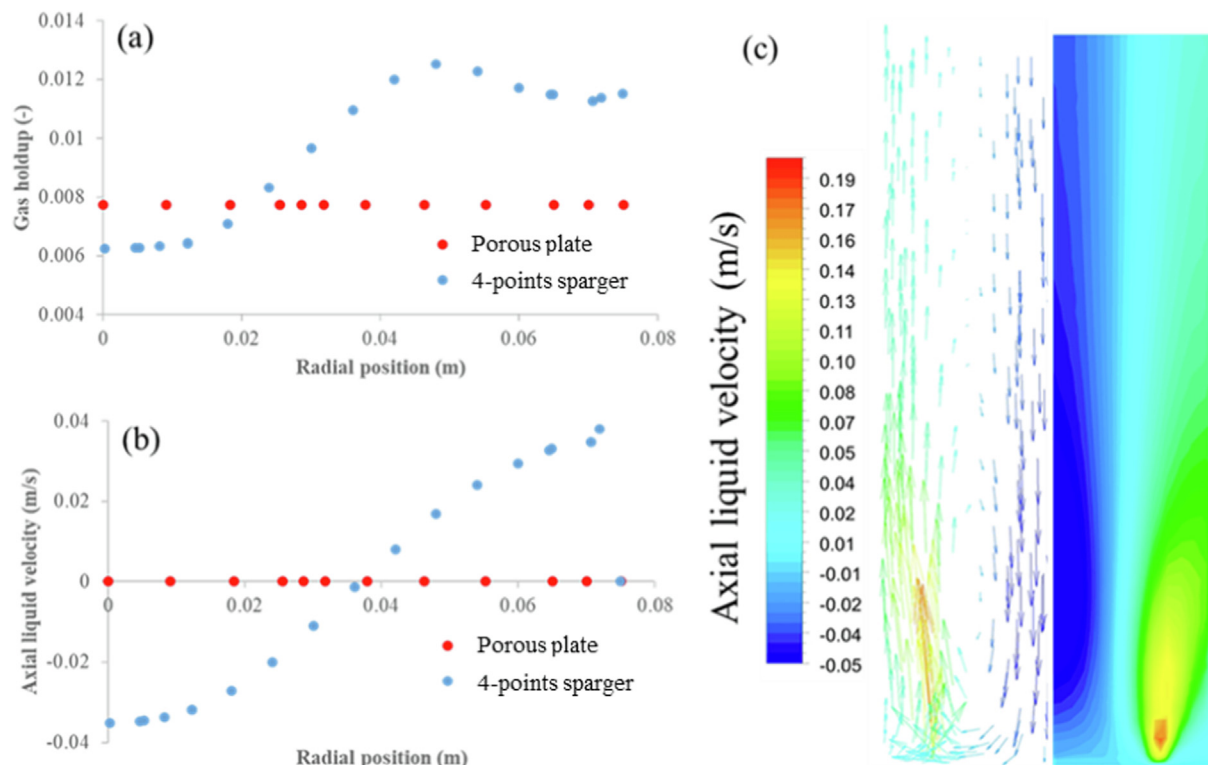


Fig. 6. Radial profile of (a) gas holdup and (b) axial liquid velocity for the reference case at $z/H = 0.25$. (c) Axial liquid velocity component contour with the velocity vector profile from the bottom up to $z/H = 0.25$ for 4-points sparger. (The number of arrows does not correspond with the mesh density).

Table 3

Hydrodynamics results ($Q_{\text{tot}} = 2.14 \text{ NL/min}$) for 1D and CFD models.

Sparger type	Numerical model	C_0	u_c	ε_G (%)	a (m^{-1})
Porous plate	CFD	–	–	0.80	24.0
	1D	1	0	0.82	24.6
4-points sparger	CFD	–	–	0.98	11.7
	1D	1.4	0.013	0.94	11.1

Table 4

Gas-side mass balance. Here $F_{i,\text{in}}$ is the molar flux of each species i in the fresh feed (before mixing with the recycling stream, see Fig. 9(a)).

Species, i	H_2	CO_2	CH_4
Inlet molar flux, $F_{i,\text{in}}$ (mol/s)	$F_{\text{H}_2,\text{in}}$	$F_{\text{CO}_2,\text{in}}$	$F_{\text{CH}_4,\text{in}}$
Outlet molar flux, $F_{i,\text{out}}$ (mol/s)	$F_{\text{H}_2,\text{in}} - \eta F_{\text{H}_2,\text{in}}$ $F_{\text{H}_2,\text{in}}(1 - \eta)$	$F_{\text{CO}_2,\text{in}} - \frac{\eta F_{\text{H}_2,\text{in}}}{4}$ $F_{\text{H}_2,\text{in}} \left(\frac{y_{\text{CO}_2,\text{in}}}{y_{\text{H}_2,\text{in}}} - \frac{\eta}{4} \right)$	$F_{\text{CH}_4,\text{in}} + \frac{\eta F_{\text{H}_2,\text{in}}}{4}$ $F_{\text{H}_2,\text{in}} \left(\frac{y_{\text{CH}_4,\text{in}}}{y_{\text{H}_2,\text{in}}} + \frac{\eta}{4} \right)$

(Zuber and Findlay, 1965). The liquid circulation velocity u_c is also computed from CFD spatially-averaged upward liquid velocity data. It describes the upward flow due to the recirculating liquid motion. As the gas holdup is low, u_c can be considered to be the superficial liquid velocity j_L in the mixture velocity of the drift-flux model $\langle j \rangle$. This assumption is reasonable as the gas holdup is very low, the liquid circulation velocity is like j_L . On the contrary, as the velocity profile is flat, C_0 for the porous plate is one from the CFD calculation. The value of u_c is considered to be zero, therefore the bubble velocity is equal to the bubble terminal velocity, as discussed in Section 2.2.

Overall, the global gas holdup computed from the 1D model closely matches that of CFD model. It shows that for the same inlet gas flow rate, the 4-points sparger yields a slightly higher gas holdup

compared with the porous plate. In contaminated system, the bubbles rise with a velocity of $0.24 \pm 0.01 \text{ m.s}^{-1}$ over a wide range of bubble sizes, leading to very close gas holdup between the two spargers. However, the interfacial area for mass transfer is higher for the porous plate due to the smaller bubble size. Table 3 reports that the interfacial area of the bubbles obtained from the porous plate is almost double that of the 4-points sparger. It is found that the sparger design has a more profound effect to the interfacial area than the gas holdup at such low superficial gas velocity ($j_G \sim \text{mm.s}^{-1}$).

3.3. Comparison of 1D and CFD model predictions with experimental data

With the hydrodynamics resolved for both 1D and CFD models, the mass transfer and bioreaction are activated to compare with the biological methanation experimental data.

Fig. 7 displays the experimental and 1D model results in terms of outlet methane purity versus methane production rate (MPR). A similar trend is observed in both spargers – lower inlet gas flow-rate leads to higher CH_4 purity but with lower productivity. It also shows that the experimental results shift to the left, signifying that a yield loss is observed when the 4-points sparger is used. To achieve a certain CH_4 purity (y -axis isoline), the productivity is always lower when the 4-points sparger is used instead of the por-

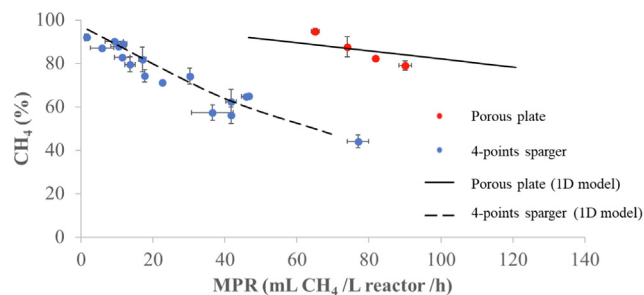


Fig. 7. Numerical prediction of both sparger performances compared with experimental data. Symbols: Experimental data from [Rafrafi et al. \(2019\)](#), Solid line: 1D model with $d_b = 2$ mm, Dashed line: 1D model with d_b fitted according to the inlet gas flowrate.

ous plate. The 1D model of the 4-points sparger case (dashed line) agrees relatively well with the experimental results, provided the inlet bubble diameter corresponds to the inlet gas flowrates. The inlet bubble diameter used varies between 3 and 5 mm in the range of experimentally imposed $Q_{G,in}$. Meanwhile, the 1D model for the porous plate results (continuous line) are obtained by setting a 2 mm inlet bubble diameter, regardless of the gas flowrate. The influence of inlet bubble diameter is discussed in [Section 3.5](#).

[Table 5](#) and [Table 6](#) summarize the overall comparison between experimental results and numerical simulations. For the same inlet gas flowrate ($Q_{G,in} = 0.14$ NL/min), use of the porous plate produces more methane (90 mL/L/h versus 77 mL/L/h experimentally) at a higher purity (80 % versus 44 % experimentally) compared with use of the 4-points sparger. For the same inlet gas flowrate, the bubble diameter for the 4-points sparger is always larger than that from the porous plate (see [Fig. 2](#)). Despite having a marginal higher gas holdup for the 4-points sparger, a larger bubble size leads to a lower interfacial area, as shown in [Fig. 8\(a\)](#) and (b). These larger bubbles generated by the 4-points sparger could be primarily due to bubble coalescence at the inlet due to much higher local gas holdup as the injection area is 56 times lower, and marginally due to the presence of a liquid recirculation cell. Consequently, low interfacial area hinders the mass transfer efficiency, leading to a lower $k_L a$ ([Fig. 8 \(c\)](#) and (d)). The spatial-averaged $k_L a$ for the porous plate case yields 113 h^{-1} , as opposed to 31 h^{-1} for the 4-points sparger case, showing an increase of 265 % in $k_L a$ by just switching the gas distributor from a non-uniform to uniform system. [Fig. 8\(e\)](#) and (f) show that the H_2 mass transfer flux is uniform and globally higher in the porous plate case than in the 4-points sparger case. A slight decrease of H_2 mass transfer flux from the inlet to the outlet is observed due to decreasing C^* , and thus a lower driving force

occurs at the top of the column. It is reported that a finer and uniform sparger is beneficial to mass transfer performance, in particular reactions which are mass transfer limited ([Möller et al., 2017](#)). Small openings and a large number of openings for the sparger have been found to promote higher interfacial area for mass transfer ([Han and Al-Dahhan, 2007](#); [Luo et al., 2011](#); [Wongwailikhit et al., 2018](#)).

At steady-state, the volume-averaged H_2 mass transfer flux for the porous plate case yields $7.83 \times 10^{-5} \text{ mol/s}$ compared with $6.42 \times 10^{-5} \text{ mol/s}$ for the 4-points sparger case. These low H_2 mass transfer fluxes are reflected in the CH_4 mole fraction profile (see [Fig. 8\(g\)](#) and (h)) whereby the upgrade of biomethane is low (roughly 80 % to 85 % and 45 % to 48 % for the porous plate and 4-points sparger, respectively), signifying that a steady-state is reached. During this stage, the bubble diameter changes insignificantly, i.e. from 2 to 2.05 mm and from 5 to 5.1 mm for the porous plate and the 4-points sparger, respectively, as predicted by the 1D model. This justifies the assumption of constant bubble diameter used in the CFD simulations. At the steady-state, the bioreaction is limited by the H_2 physical supply ([Ngu et al., 2022](#)), therefore, the description of $k_L a$ and C^* is important to capture the mass transfer flux that determines the bioreaction rate ([Schill et al., 1996](#)). An improvement in the sparger design that promotes smaller bubble size would lead to better mass transfer and a more efficient biomethane upgrading. The present 1D and CFD models obtained satisfactory results compared with the experimental data, signifying that the coupling of bubbly flow, interfacial mass transfer and bioreaction kinetics are correctly implemented.

3.4. Analytical solution of steady-state bioreactor performances

To elucidate the effect of different physical parameters involved in the bubble column on the biological efficiency, an analytical solution based on a global mass balance is derived here.

3.4.1. Calculation of methane purity ($y_{\text{CH}_4,\text{out}}$)

At steady-state, the flux-based metabolic formulation combined with the limiting flux approach imposes that the hydrogen supply is used entirely for maintenance activity, leading to $\bar{\mathbf{r}} = \{0, \bar{\varphi}_{\text{H}_2}, 0\}$, with $\bar{\varphi}_{\text{H}_2} = \frac{k_L a C_{\text{L},\text{H}_2}^*}{\epsilon_L X}$ ([Ngu et al., 2022](#)). Then, the outlet methane purity $y_{\text{CH}_4,\text{out}}$ can be derived from the mass balance of the gaseous phase. Due to the limitation of bioreaction by the H_2 mass transfer at steady-state, the local CO_2 transfer is stoichiometrically controlled by the bioreaction: with every 4 mol of H_2 transferred, 1 mol of CO_2 is transferred as well, and 1 mol of CH_4 is produced.

Table 5

Comparison of numerical model predictions with experimental data for porous plate with $Q_{G,in} = 0.14$ NL/min.

Method	H_2 (%)	CH_4 (%)	Methane Production Rate (mL/L/h)
Experiment data	10 ± 2	80 ± 2	90 ± 2
CFD model ($d_b = 2$ mm)	14	84	103
1D model ($d_b = 2 \pm 0.5$ mm)	13 ± 5	85 ± 6	83 ± 2
Analytical ($\eta_{1D} = 0.963/\eta_0 = 0.983$)	–	84/92	80/82

Table 6

Comparison of numerical model predictions with experimental data for 4-points sparger with $Q_{G,in} = 0.14$ NL/min.

Method	H_2 (%)	CH_4 (%)	Methane Production Rate (mL/L/h)
Experiment data	46 ± 3	44 ± 3	77 ± 3
CFD model ($d_b = 5$ mm)	47	48	78
1D model ($d_b = 5 \pm 0.5$ mm)	48 ± 4	48 ± 5	70 ± 3
Analytical ($\eta_{1D} = 0.808/\eta_0 = 0.82$)	–	46/47	68/69

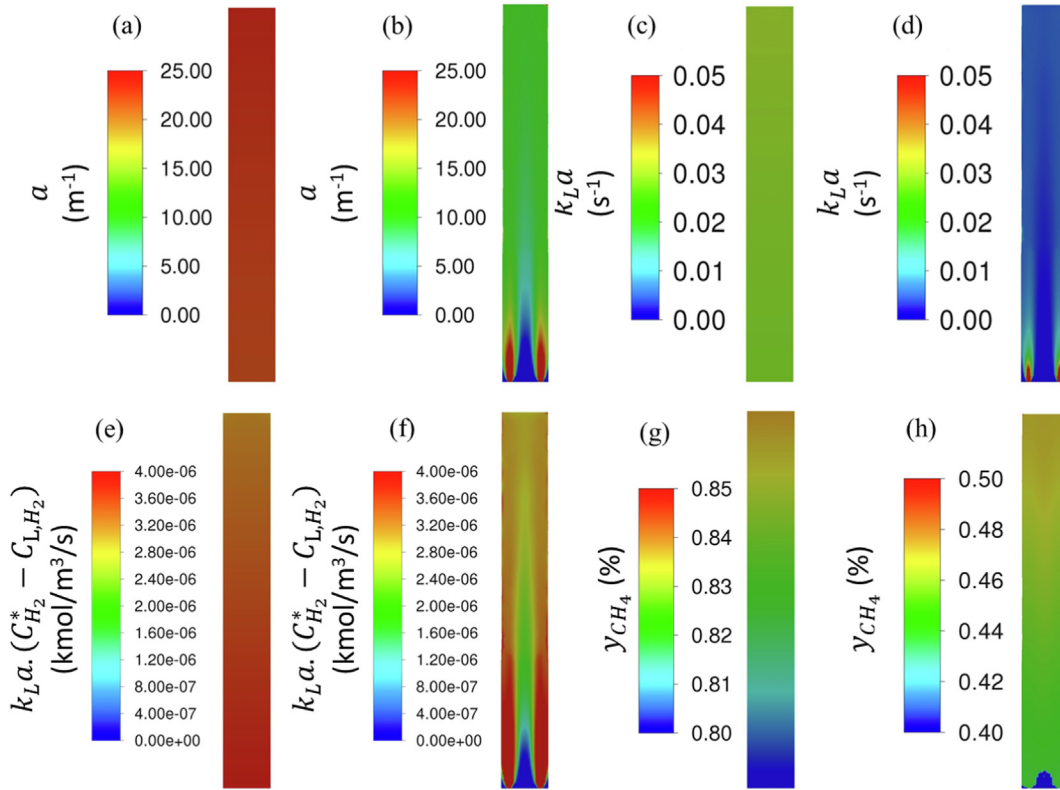


Fig. 8. Contours of interfacial area (a and b), $k_L a$ (c and d), steady-state H₂ mass transfer flux (e and f) and methane fraction (g and h) in a vertical plane passing through the center. (a), (c), (e), and (g) porous plate; (b), (d), (f) and (h) 4-points sparger.

The molar flux of each species is expressed as a function of the hydrogen conversion, η , as shown in Table 4.



η the H₂ conversion is defined as:

$$\eta = \frac{F_{H_2,in} - F_{H_2,out}}{F_{H_2,in}} = \frac{T_{H_2}}{F_{H_2,in}} \quad \eta \in [0; 1] \quad (23)$$

T_{H_2} is the overall hydrogen transfer flux in mol/s. The outlet methane purity $y_{CH_4,out}$ on a dry basis can therefore be written as:

$$y_{CH_4,out} = \frac{F_{CH_4,out}}{F_{H_2,out} + F_{CO_2,out} + F_{CH_4,out}} \quad (24)$$

Substituting the outlet molar flux of each species from Table 4 into equation (24) yields:

$$y_{CH_4,out} = \frac{\frac{y_{CH_4,in}}{y_{H_2,in}} + \frac{\eta}{4}}{(1 - \eta) + \frac{y_{CO_2,in}}{y_{H_2,in}} + \frac{y_{CH_4,in}}{y_{H_2,in}}} \quad (25)$$

Equation (25) is the general form for $y_{CH_4,out}$ prediction. In case of an inlet injection of H₂:CO₂:CH₄ ratio of 4:1:0, equation (25) is simplified to:

$$y_{CH_4,out} = \frac{\eta}{5 - 4\eta} \quad (26)$$

3.4.2. Calculation of the methane productivity (MPR)

The productivity of methane is calculated using equation (1). The outlet gas flowrate $Q_{G,out}$ must be calculated based on the mass balance from the inlet gas molar flowrate and the mass transfer fluxes. First, the outlet gas flowrate can be defined using the ideal gas law as:

$$Q_{G,out} = \frac{F_{out}RT}{P_{out}} \quad (27)$$

with F_{out} being the outlet molar flowrate in mol/s, R the ideal gas constant (8.3145 J/mol/K), T the temperature in K and P_{out} the outlet pressure in Pa. The outlet molar flowrate F_{out} can be calculated from the global mass balance as inlet molar flux $F_{in} \pm$ the mass transfer flux T_i . At steady-state, the CO₂ and CH₄ mass transfer are conditioned by the stoichiometry of the bioreaction, as stated in equation (22). Consequently, the CO₂ and CH₄ mass transfer cancel out each other, the outlet molar flowrate is written with equation (23) as:

$$F_{out} = F_{in} - T_{H_2} = F_{in} - \eta F_{H_2,in} \quad (28)$$

The inlet molar flux can be defined in terms of H₂ molar flux $F_{H_2,in}$ as:

$$F_{in} = F_{H_2,in} \left(1 + \frac{y_{CO_2,in}}{y_{H_2,in}} + \frac{y_{CH_4,in}}{y_{H_2,in}} \right) \quad (29)$$

Substituting equations (28) and (29) into (27), the outlet gas flowrate can be expressed as:

$$Q_{G,out} = \frac{F_{H_2,in} \left(1 + \frac{y_{CO_2,in}}{y_{H_2,in}} + \frac{y_{CH_4,in}}{y_{H_2,in}} - \eta \right) RT}{P_{out}} \quad (30)$$

For an inlet H₂:CO₂:CH₄ ratio of 4:1:0, and assuming a weak pressure effect for a small-scale column ($P_{out} = P_{in}$), the methane production rate MPR can be obtained by substituting equations (26) and (32) into (1), which yields equation (31).

$$MPR = \frac{1}{V} \cdot \frac{\eta}{5 - 4\eta} \cdot \left(\frac{5}{4} - \eta \right) \cdot Q_{H_2,in} = \frac{1}{V} \cdot \frac{\eta}{4} \cdot Q_{H_2,in} \quad (31)$$

with $Q_{H_2, in} = \frac{F_{H_2, in} RT}{P_{out}}$. Considering the extreme case for equations (26) and (31), whereby the ideal situation of total consumption of H_2 supply in the bioreactor ($\eta = 1$), is accompanied by total consumption of CO_2 stoichiometrically, $y_{CH_4, out}$ of 100 % will be obtained at a production rate of 25 % $Q_{H_2, in}$.

Fig. 9(b) shows that outlet methane purity $\frac{\eta}{5-4\eta}$ (blue points) increases non-linearly with η but $\frac{5}{4} - \eta$ (red points) decreases linearly with η . However, the product of the two terms, which is proportional to the methane production rate (black points) increases linearly with $\frac{\eta}{4}$. This shows that the bioreactor performances are strongly linked to the H_2 conversion rate η . The higher the H_2 mass transfer efficiency, the higher the H_2 conversion, the higher the CH_4 purity and productivity.

From equations (26) and (31), it is clear that $y_{CH_4, out}$ and MPR are a function of η , which depends on the H_2 mass transfer efficiency. The overall H_2 mass transfer flux T_{H_2} throughout the column is expressed as the volume integral of the overall mass transfer rate, or in the case of 1D model, the axial integration:

$$T_{H_2} = S \int_0^z k_L a (C_{H_2}^* - C_{L, H_2}) dz \quad (32)$$

with S being the cross-sectional area in m^2 , $k_L a$ in s^{-1} and $C_{H_2}^*$ in mol/m^3 . Equation (32) can be further simplified for a small-scale column ($H < 1$ m) where there are no non-linearities of the hydrodynamic variables in the axial direction. At steady-state, the dissolved hydrogen is depleted, thus, $C_{L, H_2} = 0$. $C_{H_2}^*$ can be calculated as $H^{cc} C_{G, H_2}$, with $H^{cc} = H_{e, H_2} RT = 0.018$ being the dimensionless Henry solubility for $T = 328.15$ K. The overall transfer flux can be estimated as:

$$T_{H_2} = S \int_0^z k_L a H^{cc} C_{G, H_2} dz \quad (33)$$

The hydrogen depletion in the gas along the column at steady-state can be described via:

$$\frac{du_G \varepsilon_G C_{G, H_2}}{dz} = -k_L a C_{H_2}^* = -k_L \frac{6\varepsilon_G}{d_b} H^{cc} C_{G, H_2} \quad (34)$$

Assuming that the gas velocity, gas holdup, and bubble diameter are kept constant, the integration of equation (34) gives the variation of H_2 mass per unit volume of reactor ($\varepsilon_G C_{G, H_2}$) along z :

$$\varepsilon_G C_{G, H_2} = \varepsilon_{G0} C_{G0, H_2} e^{-\frac{6H^{cc} k_L}{d_b u_G} z} \quad (35)$$

with $\varepsilon_{G0} C_{G0, H_2}$ being the inlet mass of H_2 per unit volume of reactor.

Substituting equations (7) and (35) into equation (33) yields:

$$T_{H_2} = S \int_0^z k_L \frac{6H^{cc}}{d_b} \varepsilon_{G0} C_{G0, H_2} e^{-\frac{6H^{cc} k_L}{d_b u_G} z} dz \quad (36)$$

The integration of equation (36) between 0 and H leads to:

$$T_{H_2} = Su_G \varepsilon_{G0} C_{G0, H_2} \left(1 - \exp\left(-\frac{6H^{cc} k_L}{d_b u_G} H\right) \right) \quad (37)$$

The term $u_G \varepsilon_{G0} C_{G0, H_2}$ can be translated as the inlet H_2 molar flux and $\exp\left(-\frac{6H^{cc} k_L}{d_b u_G} H\right)$ as the overall depletion factor throughout the column (Larsson et al., 2022). Equation (37) can be used as an estimate of the global mass transfer flux. This gives access to the calculation of hydrogen conversion through (23) and finally the methane purity through (26).

Notice that the gas holdup ε_G in the volumetric interfacial area a of equation (7) and in C_{G, H_2} of equation (35) cancel each other out when equations (7) and (35) are substituted into equation (33). This simplification of ε_G indicates clearly that no positive pressure effect on the mass transfer will be observed in bubble column. At a fixed gas mass flowrate, increasing pressure will lead to higher $C_{H_2}^*$, but the gas compression will result in lower ε_G , and thus lower interfacial area. The positive impact of pressure on $C_{H_2}^*$ is counterbalanced by the drop in interfacial area, as shown in Maalej et al. (2003). Therefore, any attempt to increase mass transfer flux by increasing pressure is fruitless. Nevertheless, high pressure is necessary in industrial-scale bubble columns as it compresses the gas to enable the treatment of higher gas loading and at the same time maintains the bubbly flow in the homogeneous regime, which is beneficial for interfacial mass transfer.

The analytical model aims to shed light on the controlling parameters involved in the biological methanation process. It highlights that the bioreactor performance of biological methanation is heavily dependent on the H_2 mass transfer efficiency (η). For example, the proposed analytical solutions for a given $H_2:CO_2$ ratio of 4:1 at the gas inlet – equations (26) and (31) highlight that both CH_4 purity and productivity are related to η , and hence T_{H_2} , which is in line with the conclusion of Schill et al. (1996). The

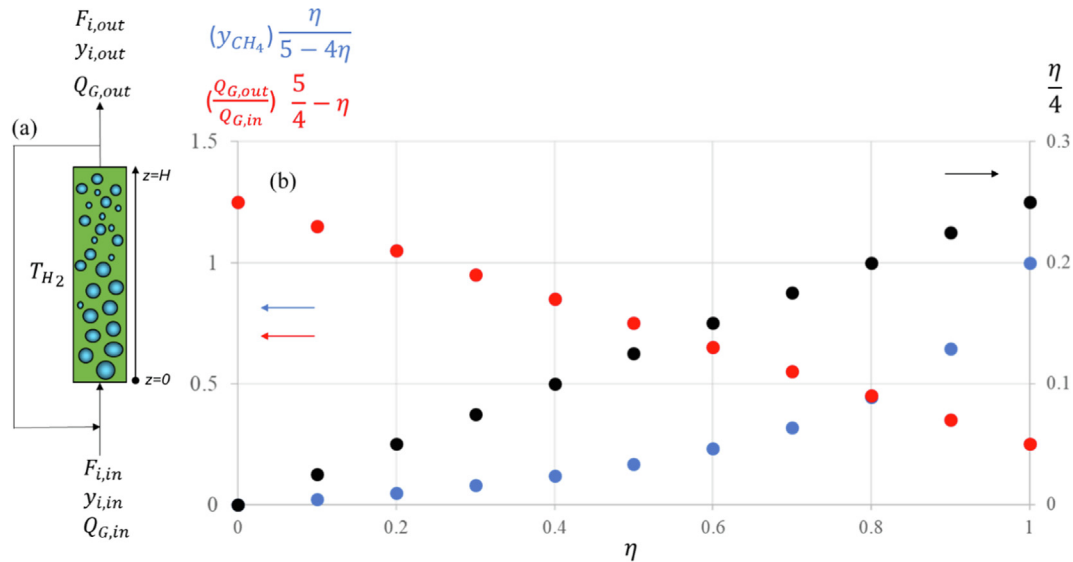


Fig. 9. (a) Schematic representation of recycling reactor (b) Effect of η on methane purity and productivity.

results are not surprising since the process operates in the H_2 mass transfer limitation regime at the stationary state. It shows that the change in $k_L a$ and C^* in the axial direction is crucial in modeling biological methanation, as the major substrates are fed to the reactor as a gaseous mixture and this physical supply can be limited by mass transfer due to poor solubility. This explains the importance of interfacial area on the biological methanation efficiency as it is related to $k_L a$ (see Fig. 8) and subsequently to d_b , u_G , and k_L . To assess correctly the overall mass transfer term T_{H_2} , a precise calculation of the spatial integration of $k_L a(C^* - C_L)$ is required. In this work, the integration of equation (32) has been assessed using the 1D model. Hence, the so-called analytical model should be interpreted as an analytical demonstration that the bioreactor performances are determined by the volume integral of the mass transfer term. If non-linearity exists, the latter has to be evaluated using accurate models, such as 1D and CFD models (Deckwer et al., 1978; Ngu et al., 2022). Otherwise, for short column ($H < 1$ m), the mass transfer can be evaluated using equation (37), by using the conditions set at the inlet for d_b , k_L , and u_G . Here, the value of η is evaluated using two approaches: 1D model or inlet conditions, denoted by η_{1D} or η_0 , respectively, as shown in Tables 5 and 6.

Table 5 and Table 6 report the bioreactor performance predicted by numerical models compared with the experimental data for the porous plate and 4-points sparger, respectively. An increase of 81 % in CH_4 purity and of 17 % in productivity is obtained experimentally when the porous plate is used over the heterogeneous sparger. For the 1D model, the results are reported with the variation of 0.5 mm on the referenced bubble diameter (2 mm for porous plate and 5 mm for 4-points sparger). For both spargers, all models slightly overpredict the methane fraction. Similarly, the CFD model overpredicts the methane production rate, whilst the 1D model underpredicts it. Overall, analytical, 1D and CFD models predict relatively well the bioreactor performances as the numerical results are close to the experimental data. A better prediction is achieved for the 4-points sparger case when the 1D model is coupled with the CFD model. This provides an efficient way to study bioreactors. Spatially resolved CFD simulations are a more efficient way to provide flow information to simpler model, such as the 1D model (Cockx et al., 1997; Siebler et al., 2020) and the compartment model (Delafosse et al., 2010; Nadal-Rey et al., 2021; Pigou and Morchain, 2015). The analytical model is interesting for small-scale column when non-linearities could be neglected. It also provides an estimation of the upper limit of the bioreactor performances, as evidenced that $\eta_0 > \eta_{1D}$; useful for performing scale-up estimations.

Upon validation with the experimental data, the analytical predictions were tested with another set of data from the work of Voelklein et al. (2019). The authors conducted similar experiments with the same configuration in a smaller bubble column (total volume of 9.5 L). The dataset of continuous ex-situ with H_2 and CO_2 as injected gases are used for comparison. The η value is given in Voelklein et al. (2019). As the $H_2:CO_2$ ratio is 4:1, equations (26) and (31) can be directly used to evaluate the CH_4 purity and productivity.

Fig. 10 presents the prediction of bioreactor performances using the analytical solution. The analytical solution agrees well with the experimental data of Voelklein et al. (2019). It also shows that the global mass balance is respected experimentally. Similar observations are drawn – higher H_2 loading leads to higher productivity but less H_2 is converted into CH_4 , leading to lower purity. When the bioreaction is limited by H_2 mass transfer, which is the case in steady-state, the biokinetics become negligible in predicting the biological production of methane, since the controlling parameters are $k_L a$ and C^* , as shown by the analytical solution.

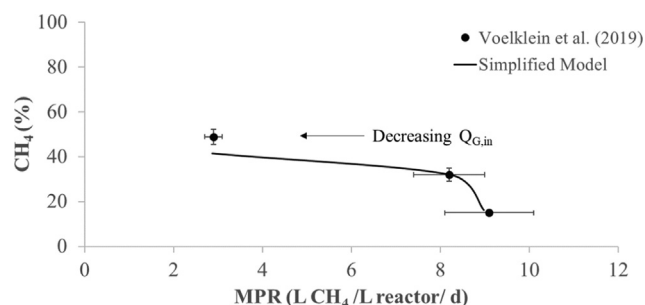


Fig. 10. Evaluation of biological methanation efficiency calculated using the analytical solution.

3.5. Sensitivity analyses on inlet gas flowrate $Q_{G,in}$, inlet bubble diameter d_b , and gas recirculation flowrate Q_r

With the 1D model validated using the experimental data, sensitivity analyses can be conducted on several operating parameters. The 1D model yields faster computation and satisfactory predictions, thus, it is useful for sensitivity analyses rather than using the computationally-intensive CFD model. The sensitivity analysis was performed for the porous plate case. This sensitivity analysis provides insights into the process phenomena important for optimization of bioreactor design. Here, the influence of inlet gas flowrate, inlet bubble diameter and gas recirculation flowrate are studied.

Fig. 11 shows that an increase in $Q_{G,in}$ leads to higher productivity. However, higher methane production does not imply higher methane purity. As shown in Fig. 11, the lower methane purity is due to a lower H_2 conversion defined in equation (23). For the same H_2 molar flux in the fresh stream $F_{H_2,in}$, the higher the $Q_{G,in}$, the lower the mass transfer efficiency, less H_2 is converted to CH_4 , thus the CH_4 purity is lower. This effect is also reported by Ghofrani-Isfahani et al. (2021) and Voelklein et al. (2019) where the authors observed an increase in CH_4 productivity is counterbalanced by a decrease in CH_4 purity when the inlet gas flowrate is increased. For the same inlet gas flowrate ($Q_{G,in} = 0.14$ NL/min), the H_2 conversion when using the 4-points sparger and porous plate is 89 % and 96 %, respectively. Therefore, higher CH_4 purity and productivity are achieved using the porous plate.

Fig. 12 shows that decreasing inlet bubble diameter leads to an increase in methane purity. Smaller bubbles offer a higher interfacial area for mass transfer, therefore a higher mass transfer efficiency (Merker et al., 2017). As the bubble diameter was not measured under bioreaction conditions, experimental measurement in air-tap water system and a literature correlation were applied to estimate the bubble diameter in real conditions. For

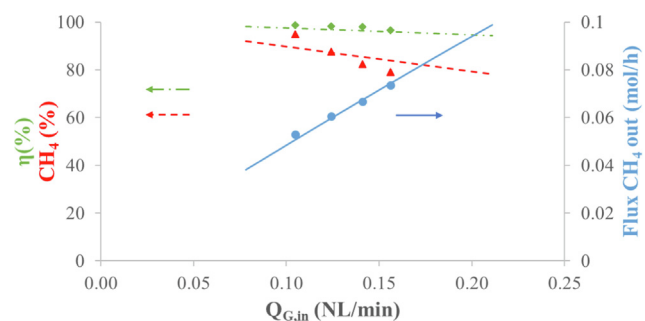


Fig. 11. Outlet methane purity (▲), H_2 conversion (◆) and methane production (●) as a function of $Q_{G,in}$. Symbols: Experimental data, Lines: 1D model with $d_b = 2$ mm.

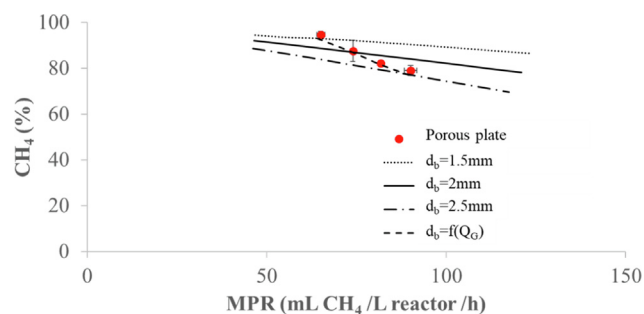


Fig. 12. Effect of inlet bubble diameter on the reactor performances using 1D model.

the porous plate, the initial bubble diameter of 2 mm is of the same order of magnitude as for previous measurements in tap water using an optical method. Under bioreaction conditions, the bubble diameter size could be reduced due to limited coalescence (Li et al., 2019; McClure et al., 2013). The bioreactor performance is sensitive to bubble diameter, as the bioreaction is limited by the mass transfer phenomenon. Analogous to a heterogeneous reaction catalyst problem, the bioreaction could be limited by the species transport and mass diffusion phenomena. These phenomena arise when the locally available specific substrate flux is insufficient to fulfill the biological demand, typically when the gas flow rate is low or when the biomass concentration is high at the steady-state, as shown in Ngu et al. (2022). Under such regimes, satisfactory descriptions of convective transport and interfacial mass transfer become crucial. The sensitivity analysis of bubble diameter for ± 0.5 mm for the reference case for both spargers was also performed and the results are reported in Table 5 and Table 6. Fig. 12 reveals that at higher $Q_{G,in}$, a better fit is obtained by a larger bubble diameter, and vice versa, similar with the observation for the 4-points sparger, as shown in Fig. 7. The gassing rate dependent inlet bubble size correlation for the porous plate is $d_b = 0.034Q_{G,in}^{1.4}$, while for the 4-points sparger is $d_b = 0.007Q_{G,in}^{0.2}$, with d_b in m and $Q_{G,in}$ in $\text{NL}\cdot\text{min}^{-1}$. This finding is consistent with the fact that the higher the $Q_{G,in}$, the larger the bubble diameter (Quintero, 2015). Also, from this study, it is observed that sparger design is pivotal for biological methanation as it determines the bubble size and subsequently defines the bioreactor performance.

Moreover, Bassani et al. (2016) and Kougias et al. (2017) have shown that increasing the gas recycling rate improves the methane purity. Fig. 13 shows that the methane purity increases when Q_r increases from 1 NL/min to 2.5 NL/min. For the same inlet H_2 molar flux, increasing the recycling flowrate leads to increasing ε_G , as more gas is present per unit volume of the bubble column. Besides, the gas residence time is also prolonged with gas recycling. In com-

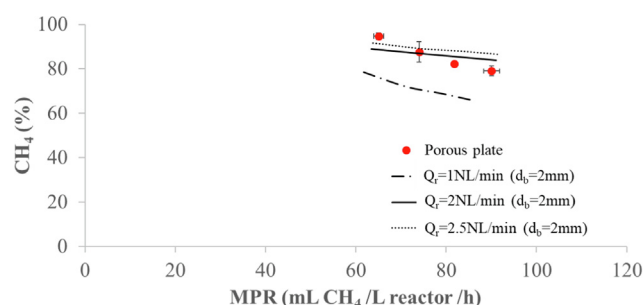


Fig. 13. Effect of gas recirculation flowrate on the reactor performances using 1D model.

bination with higher gas residence time and gas holdup, this leads to higher k_La , as more specific area is available for mass transfer, resulting in higher mass transfer efficiency, higher H_2 conversion, and thus higher methane purity. Although recycling will dilute the inlet reactive gas, lowering the saturation concentration C^* , the gain in k_La is much higher, resulting in higher overall mass transfer flux.

4. Conclusions

Successful bioconversion of H_2 and CO_2 to CH_4 was conducted in a pilot-scale bioactive bubble column. Comprehensive 1D and CFD models that couple the hydrodynamics, mass transfer and bioreaction were validated and used to predict the CH_4 purity and productivity. The results of the 1D and CFD models are consistent with the experimental data. This work aimed to demonstrate the importance of reactor design and operating conditions on H_2 mass transfer efficiency which consequently defines the biological methanation performances. It is shown that the biological methanation process is favored when a uniform porous plate is used. In terms of hydrodynamics, a marginal higher gas holdup was achieved with the 4-points porous sparger but a smaller bubble size was obtained with the porous plate. Due to uniform gas injection of the porous plate, no bubbles coalescence is expected at such low gas holdup, leading to smaller bubbles of 2 mm, as compared with the 4-points porous sparger with bubbles around 5 mm. Since the bioreaction is limited by H_2 mass transfer (due to very poor H_2 solubility), any improvement in H_2 mass transfer flux is critical to biological methanation. Therefore, having a higher interfacial area via the porous plate leads to better bioreactor performance. An increase of 265 % in k_La and subsequently 81 % in CH_4 purity is obtained when a porous plate is used instead of a 4-points sparger. However, it is less industrially applicable to use a homogeneous sintered sparger. The key is to use multiple gas spargers with large sparging area to generate bubbles as small as possible at birth and to distribute the gas the most uniformly possible to achieve better mass transfer performance.

The hydrodynamics of 4-points sparger can be described by the 1D model provided the fluid flow structure is obtained from the detailed CFD model. The 1D modelling approach leads to a simplified model which can be solved analytically and underlines the essential feature (k_La) that impacts the biological methanation process. Sensitivity analyses reveal that any improvement on the mass transfer efficiency leads to better biological methanation efficiency. On the contrary, any attempt to increase mass transfer flux by increasing pressure is fruitless as the positive impact of pressure on hydrogen solubility is counterbalanced by the negative impact on gas holdup. Nevertheless, a high pressure allows the bubble column to operate in the homogeneous bubbly regime even at higher gas loading, which is particularly critical when the biological substrate comes from the gas phase as in the biological methanation process. It is shown that any optimization of hydrodynamics, gas recirculation, bubble size and interfacial area (thus k_La) is beneficial to biological methanation.

This work shows that both the 1D and CFD models can be used to assess the impact of different parameters on the reactor performance, and thus serve as scale-up and optimization tools for biological methanation. The 1D model offers fast numerical prediction of CH_4 purity and productivity with a sufficient degree of accuracy at the pilot-scale which can be extended to industrial-scale. Previously developed metabolic flux-based model of Ngu et al. (2022) is applied here in the 1D and CFD models to couple the two-phase bubbly flow, multispecies mass transfer and biological kinetics. At the pilot-scale, the gas holdup is low and the coupling between hydrodynamics and bioreaction is rela-

tively weak, so the CFD model does not give a significant advantage over the 1D model, as shown by the almost identical results of the two models. Nevertheless, at industrial-scale, pressure effects with increasing height and longer gas residence time will have a stronger coupling with biokinetics. Complex hydrodynamics prevail in large-scale bubble columns which will subsequently impact the mass transfer and coupling with the bioreaction, as well as heterogeneities or micro-mixing limitations. From this perspective, performing numerical prediction using the CFD model becomes attractive.

CRedit authorship contribution statement

Vincent Ngu: Methodology, Conceptualization, Writing – original draft, Software, Data curation, Writing – review & editing. **David F. Fletcher:** Supervision, Software, Writing – review & editing. **John M. Kavanagh:** Supervision, Writing – review & editing. **Yan Rafrati:** Investigation. **Claire Dumas:** Investigation, Writing – review & editing. **Jérôme Morchain:** Supervision, Methodology, Conceptualization, Writing – review & editing. **Arnaud Cockx:** Supervision, Methodology, Conceptualization, Writing – review & editing.

Data availability

Data will be made available on request.

Declaration of Competing Interest

The authors declare that they have no known competing financial interests or personal relationships that could have appeared to influence the work reported in this paper.

Acknowledgments

This work benefited from a State grant managed by the Agence Nationale de la Recherche (ANR) under the Investissements d'Avenir programme with the reference ANR-18-EURE-0021. The CFD work was performed using HPC resources of CALMIP supercomputing center under the 2022 grant (P22025). The authors would like to acknowledge Claude Le Men for his technical support for the optical setup for bubble image acquisition. The experimental work was conducted thanks to funding received from the Occitanie French Region, and the French ecological transition agency (ADEME) in the framework of HYCABIOME and HYDROMET projects.

References

- Abro, M., Yu, L., Yu, G., Chen, X., Qazi, A.B., 2021. Experimental investigation of hydrodynamic parameters and bubble characteristics in CO₂ absorption column using pure ionic liquid and binary mixtures: effect of porous sparger and operating conditions. *Chem. Eng. Sci.* 229, <https://doi.org/10.1016/j.ces.2020.116041> 116041.
- Amaral, A., Gillot, S., Garrido-Baserba, M., Filali, A., Karpinska, A.M., Plósz, B.G., De Groot, C., Bellandi, G., Nopens, I., Takács, I., Lizarralde, I., Jimenez, J.A., Fiat, J., Rieger, L., Arnell, M., Andersen, M., Jeppsson, U., Rehman, U., Fayolle, Y., Amerlinck, Y., Rosso, D., 2019. Modelling gas-liquid mass transfer in wastewater treatment: when current knowledge needs to encounter engineering practice and vice versa. *Water Sci. Technol.* 80, 607–619. <https://doi.org/10.2166/wst.2019.253>.
- Angelidaki, I., Treu, L., Tsapekos, P., Luo, G., Campanaro, S., Wenzel, H., Kougias, P.G., 2018. Biogas upgrading and utilization: current status and perspectives. *Biotechnol. Adv.* 36, 452–466. <https://doi.org/10.1016/j.biotechadv.2018.01.011>.
- Bassani, I., Kougias, P.G., Angelidaki, I., 2016. In-situ biogas upgrading in thermophilic granular UASB reactor: key factors affecting the hydrogen mass transfer rate. *Bioresour. Technol.* 221, 485–491. <https://doi.org/10.1016/j.biortech.2016.09.083>.
- Bassani, I., Kougias, P.G., Treu, L., Porté, H., Campanaro, S., Angelidaki, I., 2017. Optimization of hydrogen dispersion in thermophilic up-flow reactors for ex situ biogas upgrading. *Bioresour. Technol.* 234, 310–319. <https://doi.org/10.1016/j.biortech.2017.03.055>.
- Bauer, M., Eigenberger, G., 1999. A concept for multi-scale modeling of bubble columns and loop reactors. *Chem. Eng. Sci.* 54, 5109.
- Besagni, G., Gallazzini, L., Inzoli, F., 2018. Effect of gas sparger design on bubble column hydrodynamics using pure and binary liquid phases. *Chem. Eng. Sci.* 176, 116–126. <https://doi.org/10.1016/j.ces.2017.10.036>.
- Cockx, A., Liné, A., Roustan, M., Do-Quang, Z., Lazarova, V., 1997. Numerical simulation and physical modeling of the hydrodynamics in an air-lift internal loop reactor. *Chem. Eng. Sci.* 52, 3787–3793. [https://doi.org/10.1016/S0009-2509\(97\)00224-8](https://doi.org/10.1016/S0009-2509(97)00224-8).
- Deckwer, W.-D., Adler, I., Zaidi, A., 1978. A comprehensive study on co₂-interphase mass transfer in vertical cocurrent and countercurrent gas-liquid flow. *Can. J. Chem. Eng.* 56, 43–55. <https://doi.org/10.1002/cjce.5450560107>.
- Deckwer, W.-D., Burckhart, R., Zoll, G., 1974. Mixing and mass transfer in tall bubble columns. *Chem. Eng. Sci.* 29, 2177–2188. [https://doi.org/10.1016/0009-2509\(74\)80025-4](https://doi.org/10.1016/0009-2509(74)80025-4).
- Deen, N.G., Solberg, T., Hjertager, B.H., 2001. Large eddy simulation of the Gas-Liquid flow in a square cross-sectioned bubble column. In: *Chemical Engineering Science, Proceedings of the 5th International Conference on Gas-Liquid and Gas-Liquid-Solid Reactor Engineering* 56, 6341–6349. doi: 10.1016/S0009-2509(01)00249-4.
- Delafosse, A., Delvigne, F., Collignon, M., Crine, M., Thonart, P., Toye, D., 2010. Development of a compartment model based on CFD simulations for description of mixing in bioreactors <https://popups.uliege.be/1780-4507/index.php?id=6139>.
- Díaz, I., Pérez, C., Alfaro, N., Fdz-Polanco, F., 2015. A feasibility study on the bioconversion of CO₂ and H₂ to biomethane by gas sparging through polymeric membranes. *Bioresour. Technol.* 185, 246–253. <https://doi.org/10.1016/j.biortech.2015.02.114>.
- European Commission, 2016a. 2030 climate & energy framework [WWW Document]. Climate Action - European Commission. URL https://ec.europa.eu/clima/policies/strategies/2030_en (accessed 9.29.21).
- European Commission, 2016b. Paris Agreement [WWW Document]. Climate Action - European Commission. URL https://ec.europa.eu/clima/policies/international/negotiations/paris_en (accessed 9.29.21).
- Fayolle, Y., Cockx, A., Gillot, S., Roustan, M., Héduit, A., 2007. Oxygen transfer prediction in aeration tanks using CFD. In: *Chemical Engineering Science, 8th International Conference on Gas-Liquid and Gas-Liquid-Solid Reactor Engineering* 62, 7163–7171. doi: 10.1016/j.ces.2007.08.082.
- Figueroa, J., Benbelkacem, H., Dumas, C., Buffiere, P., 2021. Biomethanation of syngas by enriched mixed anaerobic consortium in pressurized agitated column. *Bioresour. Technol.* 338, <https://doi.org/10.1016/j.biortech.2021.125548> 125548.
- Ghofrani-Isfahani, P., Tsapekos, P., Peprah, M., Kougias, P., Zhu, X., Kovalovszki, A., Zervas, A., Zha, X., Jacobsen, C.S., Angelidaki, I., 2021. Ex-situ biogas upgrading in thermophilic up-flow reactors: the effect of different gas diffusers and gas retention times. *Bioresour. Technol.* 340, <https://doi.org/10.1016/j.biortech.2021.125694> 125694.
- Han, L., Al-Dahhan, M.H., 2007. Gas-liquid mass transfer in a high pressure bubble column reactor with different sparger designs. *Chem. Eng. Sci. Fluidized Bed Appl.* 62, 131–139. <https://doi.org/10.1016/j.ces.2006.08.010>.
- Harteveld, W.K., Mudde, R.F., Van Den Akker, H.E.A., 2003. Dynamics of a bubble column: influence of gas distribution on coherent structures. *Can. J. Chem. Eng.* 81, 389–394. <https://doi.org/10.1002/cjce.5450810308>.
- Higbie, R., 1935. The rate of absorption of a pure gas into a still liquid during short periods of exposure. *Trans. AIChE* 31, 365–389.
- Jensen, M.B., Ottosen, L.D.M., Kofoed, M.V.W., 2021. H₂ gas-liquid mass transfer: a key element in biological Power-to-Gas methanation. *Renew. Sustain. Energy Rev.* 147, <https://doi.org/10.1016/j.rser.2021.111209> 111209.
- Kougias, P.G., Treu, L., Benavente, D.P., Boe, K., Campanaro, S., Angelidaki, I., 2017. Ex-situ biogas upgrading and enhancement in different reactor systems. *Bioresour. Technol.* 225, 429–437. <https://doi.org/10.1016/j.biortech.2016.11.124>.
- Kulkarni, A.V., Joshi, J.B., 2011. Design and selection of sparger for bubble column reactor. Part I: performance of different spargers. *Chem. Eng. Res. Des.* 89, 1972–1985. <https://doi.org/10.1016/j.cherd.2011.01.004>.
- Laguillaumie, L., Rafrati, Y., Moya-Leclair, E., Delagnes, D., Dubos, S., Spérandio, M., Paul, E., Dumas, C., 2022. Stability of ex situ biological methanation of H₂/CO₂ with a mixed microbial culture in a pilot scale bubble column reactor. *Bioresour. Technol.* 354, <https://doi.org/10.1016/j.biortech.2022.127180> 127180.
- Lardon, L., Thorberg, D., Krosgaard, L., 2018. Biogas valorization and efficient energy management [WWW Document]. URL <http://powerstep.eu/system/files/generated/files/resource/d3-2-technical-and-economic-analysis-of-biological-methanationdeliverable.pdf>.
- Larsson, T., Duran Quintero, C., Gillot, S., Cockx, A., Fayolle, Y., 2022. Development and validation of a comprehensive 1-D model to simulate gas hold-up and gas-liquid transfer in deep air-water bubble columns. *Chem. Eng. Sci.* 248, <https://doi.org/10.1016/j.ces.2021.117210> 117210.
- Lecker, B., Illi, L., Lemmer, A., Oechsner, H., 2017. Biological hydrogen methanation – a review. *Bioresour. Technol.* 245, 1220–1228. <https://doi.org/10.1016/j.biortech.2017.08.176>.
- Lee, J.C., Kim, J.H., Chang, W.S., Pak, D., 2012. Biological conversion of CO₂ to CH₄ using hydrogenotrophic methanogen in a fixed bed reactor. *J. Chem. Technol. Biotechnol.* 87, 844–847. <https://doi.org/10.1002/jctb.3787>.

- Leonzio, G., 2018. Study of mixing systems and geometric configurations for anaerobic digesters using CFD analysis. *Renew. Energy* 123, 578–589. <https://doi.org/10.1016/j.renene.2018.02.071>.
- Leonzio, G., 2016. Biological Sabatier reaction with CFD analysis. *AIP Conf. Proc.* 1790, <https://doi.org/10.1063/1.4968767> 150028.
- Li, L., Zhao, Y., Lian, W., Han, C., Zhang, Q., Huang, W., 2021. Review on the effect of gas distributor on flow behavior and reaction performance of the bubble/slurry reactors. *Ind. Eng. Chem. Res.* 60, 10835–10853. <https://doi.org/10.1021/acs.iecr.1c00609>.
- Li, X., Griffin, D., Li, X., Henson, M.A., 2019. Incorporating hydrodynamics into spatiotemporal metabolic models of bubble column gas fermentation. *Biotechnol. Bioeng.* 116, 28–40. <https://doi.org/10.1002/bit.26848>.
- Luo, G., Angelidaki, I., 2013. Hollow fiber membrane based H₂ diffusion for efficient in situ biogas upgrading in an anaerobic reactor. *Appl. Microbiol. Biotechnol.* 97, 3739–3744. <https://doi.org/10.1007/s00253-013-4811-3>.
- Luo, L., Liu, F., Xu, Y., Yuan, J., 2011. Hydrodynamics and mass transfer characteristics in an internal loop airlift reactor with different spargers. *Chem. Eng. J.* 175, 494–504. <https://doi.org/10.1016/j.cej.2011.09.078>.
- Maalej, S., Benadda, B., Otterbein, M., 2003. Interfacial area and volumetric mass transfer coefficient in a bubble reactor at elevated pressures. *Chem. Eng. Sci.* 58, 2365–2376. [https://doi.org/10.1016/S0009-2509\(03\)00085-X](https://doi.org/10.1016/S0009-2509(03)00085-X).
- Markthaler, S., Plankenbühler, T., Weidlich, T., Neubert, M., Karl, J., 2020. Numerical simulation of trickle bed reactors for biological methanation. *Chem. Eng. Sci.* 226, <https://doi.org/10.1016/j.ces.2020.115847> 115847.
- Martin, M.R., Fornero, J.J., Stark, R., Mets, L., Angenent, L.T., 2013. A single-culture bioprocess of methanotermobacter thermotrophicus to upgrade digester biogas by CO₂-to-CH₄ conversion with H₂ [WWW Document]. *Archaea*. <https://doi.org/10.1155/2013/157529>.
- McClure, D.D., Kavanagh, J.M., Fletcher, D.F., Barton, G.W., 2014. Development of a CFD model of bubble column bioreactors: part two – comparison of experimental data and CFD predictions. *Chem. Eng. Technol.* 37, 131–140. <https://doi.org/10.1002/ceat.201300546>.
- McClure, D.D., Kavanagh, J.M., Fletcher, D.F., Barton, G.W., 2013. Development of a CFD model of bubble column bioreactors: part one – a detailed experimental study. *Chem. Eng. Technol.* 36, 2065–2070. <https://doi.org/10.1002/ceat.201300544>.
- Merker, D., Böhm, L., Oßberger, M., Klüfers, P., Kraume, M., 2017. Mass transfer in reactive bubbly flows – a single-bubble study. *Chem. Eng. Technol.* 40, 1391–1399. <https://doi.org/10.1002/ceat.201600715>.
- Möller, F., Seiler, T., Lau, Y.M., Weber, M.F., Weber, M.K., Hampel, U., Schubert, M., 2017. Performance comparison between different sparger plate orifice patterns: Hydrodynamic investigation using ultrafast X-ray tomography. *Chem. Eng. J.* 316, 857–871. <https://doi.org/10.1016/j.cej.2017.01.114>.
- Nadal-Rey, G., McClure, D.D., Kavanagh, J.M., Cassells, B., Cornelissen, S., Fletcher, D. F., Gernaey, K.V., 2022. Computational fluid dynamics modelling of hydrodynamics, mixing and oxygen transfer in industrial bioreactors with Newtonian broths. *Biochem. Eng. J.* 177, <https://doi.org/10.1016/j.bej.2021.108265> 108265.
- Nadal-Rey, G., McClure, D.D., Kavanagh, J.M., Cassells, B., Cornelissen, S., Fletcher, D. F., Gernaey, K.V., 2021. Development of dynamic compartment models for industrial aerobic fed-batch fermentation processes. *Chem. Eng. J.* 420, <https://doi.org/10.1016/j.cej.2021.130402> 130402.
- Ngu, V., Morchain, J., Cockx, A., 2022. Spatio-temporal 1D gas–liquid model for biological methanation in lab scale and industrial bubble column. *Chem. Eng. Sci.* 251, <https://doi.org/10.1016/j.ces.2022.117478> 117478.
- Peillex, J.-P., Fardeau, M.-L., Belaich, J.-P., 1990. Growth of *Methanobacterium thermoautotrophicum* on H₂/CO₂: high CH₄ productivities in continuous culture. *Biomass* 21, 315–321. [https://doi.org/10.1016/0144-4565\(90\)90080-4](https://doi.org/10.1016/0144-4565(90)90080-4).
- Pigou, M., Morchain, J., 2015. Investigating the interactions between physical and biological heterogeneities in bioreactors using compartment, population balance and metabolic models. *Chem. Eng. Sci.* 126, 267–282. <https://doi.org/10.1016/j.ces.2014.11.035>.
- Quintero, C.D., 2015. Comportement rhéologique des boues activées: Mesures, modélisation et impact sur le transfert d'oxygène dans les bioréacteurs aérés (phdthesis). INSA de Toulouse.
- Rafrafi, Y., Contreras, V., Lefebvre, X., Mengelle, E., Delagnes, D., Dubos, S., Spérandio, M., Palmade, S., Guérre, V., Dumas, C., 2019. Développement et optimisation d'un procédé de méthanation biologique. Presented at the SFGP 2019, Nantes, France.
- Rafrafi, Y., Laguillaumie, L., Dumas, C., 2020. Biological Methanation of H₂ and CO₂ with mixed cultures: current advances, hurdles and challenges. *Waste Biomass Valor.* doi: 10.1007/s12649-020-01283-z.
- Rusmanis, D., O'Shea, R., Wall, D.M., Murphy, J.D., 2019. Biological hydrogen methanation systems – an overview of design and efficiency. *Bioengineered* 10, 604–634. <https://doi.org/10.1080/21655979.2019.1684607>.
- Schill, N., van Gulik, W.M., Voisard, D., von Stockar, U., 1996. Continuous cultures limited by a gaseous substrate: development of a simple, unstructured mathematical model and experimental verification with *Methanobacterium thermoautotrophicum*. *Biotechnol. Bioeng.* 51, 645–658. [https://doi.org/10.1002/\(SICI\)1097-0290\(19960920\)51:6<645::AID-BIT4>3.0.CO;2-H](https://doi.org/10.1002/(SICI)1097-0290(19960920)51:6<645::AID-BIT4>3.0.CO;2-H).
- Sharaf, S., Zednikova, M., Ruzicka, M.C., Azzopardi, B.J., 2016. Global and local hydrodynamics of bubble columns – effect of gas distributor. *Chem. Eng. J.* 288, 489–504. <https://doi.org/10.1016/j.cej.2015.11.106>.
- Siebler, F., Lapin, A., Takors, R., 2020. Synergistically applying 1-D modeling and CFD for designing industrial scale bubble column syngas bioreactors. *Eng. Life Sci.* 20, 239–251. <https://doi.org/10.1002/elsc.201900132>.
- Sieborg, M.U., Jønson, B.D., Ashraf, M.T., Yde, L., Triolo, J.M., 2020. Biomethanation in a thermophilic biotrickling filter using cattle manure as nutrient media. *Bioresour. Technol. Rep.* 9, <https://doi.org/10.1016/j.biteb.2020.100391> 100391.
- Simonin, O., Viollet, P.L., 1990. Prediction of an oxygen droplet pulverization in a compressible subsonic coflowing hydrogen flow. *ASME. FED (American Society of Mechanical Engineers, Fluids Engineering Division)* 91, 73–82.
- Strübing, D., Moeller, A.B., Mößnang, B., Leubner, M., Drewes, J.E., Koch, K., 2018. Anaerobic thermophilic trickle bed reactor as a promising technology for flexible and demand-oriented H₂/CO₂ biomethanation. *Appl. Energy* 232, 543–554. <https://doi.org/10.1016/j.apenergy.2018.09.225>.
- Tabib, M.V., Roy, S.A., Joshi, J.B., 2008. CFD simulation of bubble column—an analysis of interphase forces and turbulence models. *Chem. Eng. J.* 139, 589–614. <https://doi.org/10.1016/j.cej.2007.09.015>.
- Talvy, S., Cockx, A., Liné, A., 2007. Modeling hydrodynamics of gas–liquid airlift reactor. *AIChE J.* 53, 335–353. <https://doi.org/10.1002/aic.11078>.
- Thibodeaux, L.J., Mackay, D. (Eds.), 2010. *Handbook of Chemical Mass Transport in the Environment*. CRC Press, Boca Raton. doi: 10.1201/b10262.
- Tomiyama, A., Kataoka, I., Zun, I., Sakaguchi, T., 1998. Drag coefficients of single bubbles under normal and micro gravity conditions. *JSM Int. J. Ser. B* 41, 472–479. <https://doi.org/10.1299/jsmeb.41.472>.
- Tomiyama, T., Tama, H., Zun, I., Hosokawa, S., 2002. Transverse migration of single bubbles in simple shear flows. *Chem. Eng. Sci.* 57, 1849–1858. doi: 10.1016/S0009-2509(02)00085-4.
- Ullrich, T., Lemmer, A., 2019. Performance enhancement of biological methanation with trickle bed reactors by liquid flow modulation. *GCB Bioenergy* 11, 63–71. <https://doi.org/10.1111/gcbb.12547>.
- Ullrich, T., Lindner, J., Bär, K., Mörs, F., Graf, F., Lemmer, A., 2018. Influence of operating pressure on the biological hydrogen methanation in trickle-bed reactors. *Bioresour. Technol.* 247, 7–13. <https://doi.org/10.1016/j.biortech.2017.09.069>.
- Veera, U.P., Joshi, J.B., 1999. Measurement of gas hold-up profiles by gamma ray tomography: effect of sparger design and height of dispersion in bubble columns. *Chem. Eng. Res. Des.* 77, 303–317. <https://doi.org/10.1205/026387699526232>.
- Voelklein, M.A., Rusmanis, D., Murphy, J.D., 2019. Biological methanation: Strategies for in-situ and ex-situ upgrading in anaerobic digestion. *Appl. Energy* 235, 1061–1071. <https://doi.org/10.1016/j.apenergy.2018.11.006>.
- Wachi, S., Nojima, Y., 1990. Gas-phase dispersion in bubble columns. *Chem. Eng. Sci.* 45, 901–905. [https://doi.org/10.1016/0009-2509\(90\)85012-3](https://doi.org/10.1016/0009-2509(90)85012-3).
- Wongwailikhit, K., Warunyuwong, P., Chawaloephonsiya, N., Dietrich, N., Hébrard, G., Painmanakul, P., 2018. Gas sparger orifice sizes and solid particle characteristics in a bubble column – relative effect on hydrodynamics and mass transfer. *Chem. Eng. Technol.* 41, 461–468. <https://doi.org/10.1002/ceat.201700293>.
- Zuber, N., Findlay, J.A., 1965. Average volumetric concentration in two-phase flow systems. *J. Heat Transfer* 87, 453–468. <https://doi.org/10.1115/1.3689137>.